GIA-based sea level change due to Marinoan snowball Earth deglaciation

入江, 芳矢

https://doi.org/10.15017/4060001

出版情報：九州大学, 2019, 博士（理学）, 課程博士
バージョン：
権利関係：

GIA-based sea level change due to Marinoan snowball Earth deglaciation

Yoshiya Irie

Department of Earth and Planetary Sciences, Graduate School of Science,
Kyushu University

February, 2020

Abstract

Marinoan snowball Earth offers us a set of sedimentary and geochemical records for exploring glacial isostatic adjustment (GIA) associated with one of the most severe glaciations in Earth history. An accurate prediction of GIA-based relative sea level (RSL) change associated with a snowball Earth meltdown will help to explore sedimentary records for RSL changes and to place independent constraints on mantle viscosity and on the durations of syn-deglaciation (T_d) and cap carbonate deposition. Here we mainly examine post-deglacial RSL change characterized by an RSL drop and a resumed transgression inferred from the cap dolostones on the continental shelf in South China. Such a non-monotonic RSL behavior may be a diagnostic GIA-signal for the Marinoan deglaciation resulting from a significantly longer post-deglacial GIA-response than that for the last deglaciation. A post-deglacial RSL drop followed by transgression in South China, which is significantly affected by Earth's rotation, is predicted over the continental shelf for models with $T_d \leq 20$ kyr and a deep mantle viscosity of $\sim 5 \times 10^{22}$ Pa s regardless of the upper mantle viscosity. The inferred GIA model also explains the post-deglacial RSL changes such as sedimentary-inferred RSL drops on the continental shelf in northwestern Canada and California at low-latitude regions insignificantly affected by Earth's rotation. Furthermore, the good match between the predicted and observed RSL changes in South China suggests an approximate duration of ~50 kyr for the Marinoan ^{17}O depletion event, an atmospheric event linked to the post-Marinoan drawdown of CO_2 and the concurrent rise of O_2.

Contents

Chapter 1

General Introduction

1.1 Snowball Earth and cap carbonate

"Snowball Earth", in which the Earth was almost entirely covered by ice, has been proposed for glaciations in the Neoproterozoic Era (see reviews by Hoffman & Schrag, 2002; Hoffman et al., 2017). It is accepted that the last snowball Earth occurred during the Marinoan glaciation, which ended at ~635 million years ago (Ma). Marinoan glacial deposits, which were formed by glaciers that extended to sea level at low latitudes, are sharply overlain by carbonate rocks, called "cap carbonates" or "cap dolostones" (Figure 1.1). Cap carbonates can be related to snowball Earth. Once snowball Earth occurs, volcanically outgassed CO_2 must accumulate to very high concentration over millions to tens of millions of years in order to overcome the cooling effect of ice albedo and trigger deglaciation. However, once the deglaciation begins, it proceeds rapidly due mainly to ice albedo feedback. In the resulting hothouse climate, enhanced weathering provides large inputs of alkalinity to the ocean, leading to rapid carbonate precipitation. This process consumes atmospheric CO_2 until a new steady state is reached. Cap carbonates are important for understanding the recovery of the Earth system from a snowball state. This thesis explores sea level changes inferred from the deposition of cap carbonates.

Figure 1.1. Marinoan glacial deposit and overlaying cap carbonate, Otavi group, Namibia. Adopted from Hoffman et al. (2017).

1.2 Glacial isostatic adjustment

The knowledge of the sea level changes following the Last Glacial Maximum (LGM, ~21 kyr before the present (BP)) would be instructive in considering sea level variations associated with Marinoan snowball deglaciation. During the LGM, much of North America and Northern Europe were covered by thick ice sheets (Figure 1.2a). These ice sheets vanished by ~6 kyr BP. During the last deglaciation, water mass is transferred from the ice sheets to the ocean, causing an equivalent sea level (ESL) rise of ~130 m (Figure 1.2b). The removal of the ice load results in a rebound of the surface in order to restore isostasy. On the other hand, the ocean loading depressed the surface below. The response of the Earth to changes in surface loading is referred to as glacial isostatic adjustment (GIA). Observations related to GIA due to the last deglaciation have provided constraints on the Earth's viscosity structure and the history of the ice sheet change. One such GIA-related observations is sea level change, which is preserved in the geological record as a shoreline migration or a change in

water depth. Sea level change is caused by ESL change as well as GIA processes such as vertical motions of the Earth's surface and gravity field. Moreover, GIA causes changes in Earth's rotational axis and these changes feedback on sea level change. Accurate modeling for sea level change due to GIA is important for inferring the Earth's viscosity structure and the ice sheet change.

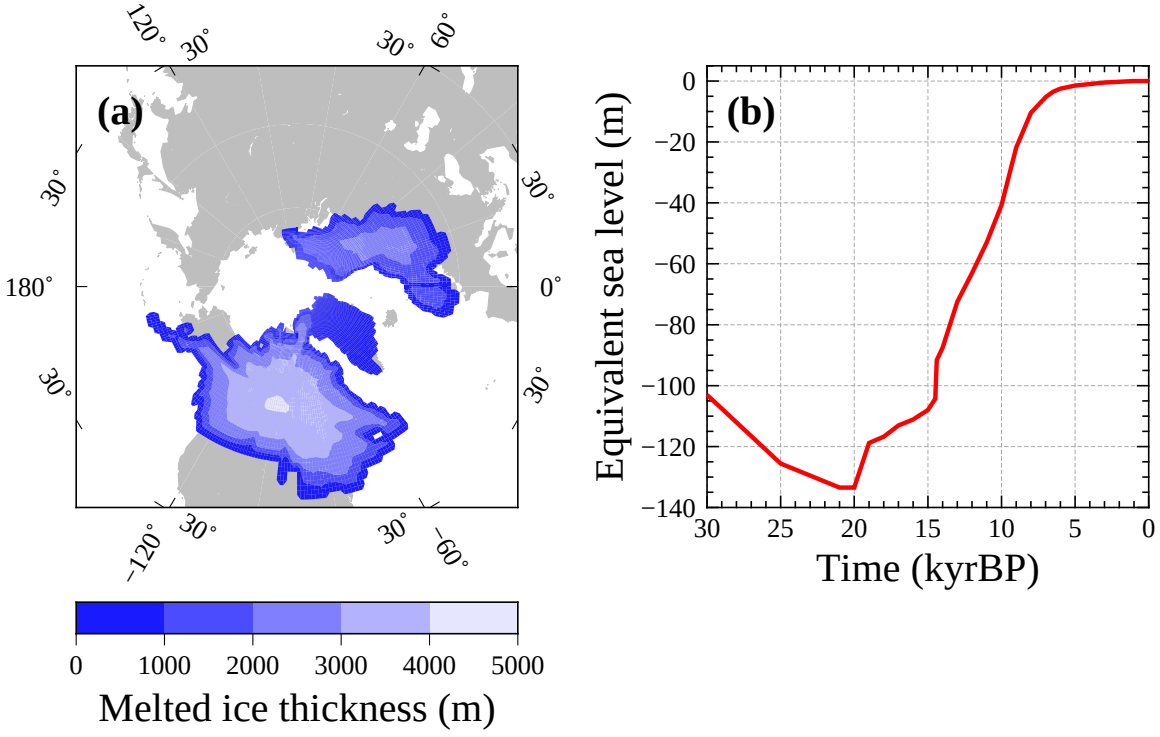

Figure 1.2. (a) Spatial distribution of total melted ice thicknesses during the last deglaciation for the Northern Hemisphere ice sheets of IA20 ice model by Nakada & Okuno (2017). (b) The equivalent sea level (ESL) history for IA20 ice model. The ESL is defined by the change in meltwater volume divided by the surface area of the ocean at the present day.

We briefly outline mantle viscosity structure inferred from GIA studies associated with the last deglaciation (see a review for mantle viscosity by Forte, 2015). Many GIA studies have adopted a simple three-layer viscosity model characterized by elastic lithosphere thickness, upper mantle viscosity above 670 km depth and lower mantle viscosity. It is a general agree-

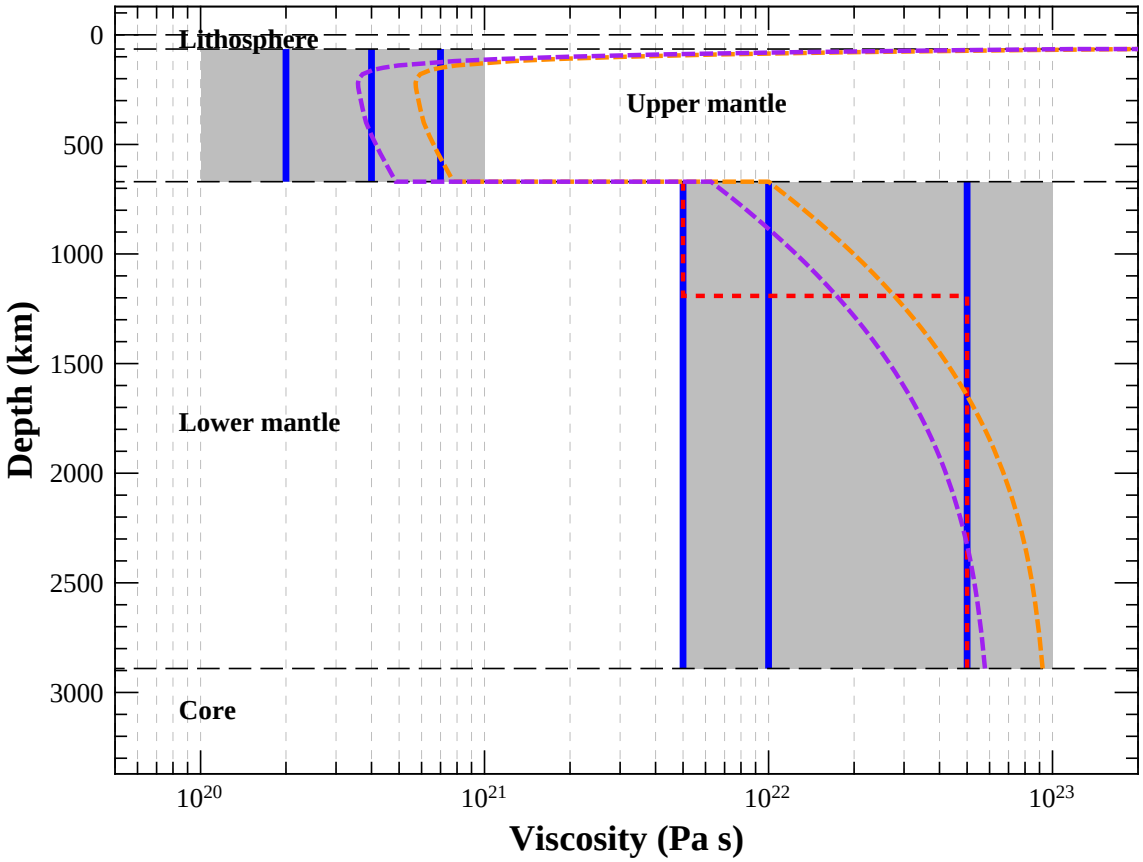

Figure 1.3. Viscosity profiles in the mantle. The gray regions represent a range of mantle viscosity inferred from GIA studies associated with the last deglaciation. Blue and red dotted lines show viscosity models adopted in Chapter 3. Orange dashed line shows the viscosity model preferred by Nakada et al. (2018), and the viscosity model with temperature distribution ~50 K higher than that is shown by purple dashed line.

ment that the lower mantle viscosity (5×10^{21}–10^{23} Pa s) is higher than the upper mantle viscosity (10^{20}–10^{21} Pa s) (Figure 1.3). On the other hand, some recent GIA sudies have yielded a deep mantle viscosity of $\sim 10^{23}$ Pa s adopting a more complex lower mantle viscosity structure (Lau et al., 2016; Nakada & Okuno, 2016). Most recent study by Nakada et al. (2018) examined the GIA-related observations such as sea level changes and secular rate of change of the degree-two zonal harmonic of the geopotential, $\dot{J}_2$, based on a depth-dependent

viscosity model with an exponential profile described by temperature, pressure, activation energy, and activation volume. Their preferred viscosity structure is described by a laterally heterogeneous upper mantle viscosity of (1–10) $\times$ 10^{20} Pa s, $\sim 10^{22}$ Pa s at 670 km depth (a significant viscosity jump at 670 km depth), and smooth depth variation in the lower mantle viscosity (an order of gradual increase).

1.3 Structure of this thesis

In Chapter 2, we describe the mathematical formulation for modeling the Earth response to surface loading, GIA-induced variations in Earth's rotation, and sea level change due to GIA. In Chapter 3, we examine sea level changes due to the Marinoan snowball Earth deglaciation, which are inferred from cap carbonates, and try to put some constraints on Marinoan mantle viscosity structure and the durations of deglaciation and cap carbonate deposition, the last two of which are linked to the rate of atmospheric CO_2 drawdown.

Chapter 2

Mathematical formulatoin

2.1 Solid Earth deformation

This section deals with the viscoelastic response of the solid Earth to external forces, and the response is described by the Love numbers. The formulation follows that of Wu & Peltier (1982) and Chapter 1 of Sabadini et al. (2016).

2.1.1 Field equations

The equation of motion is

$$0 = -\rho \boldsymbol{\nabla} \phi + \boldsymbol{\nabla} \cdot \boldsymbol{\sigma} \tag{2.1}$$

wherer ρ is the density, ϕ is the graviational potential, and $\boldsymbol{\sigma}$ is the stress tensor. The gravitatioanal potential satisfies the Poisson's equation

$$\boldsymbol{\nabla}^2 \phi = 4\pi G \rho \tag{2.2}$$

where G is the gravitational constatnt.

We assume that the initial state is in a hydrostatic equilibrium. The total fields $\boldsymbol{\sigma}$, ϕ, and ρ

are decomposed into the initial fields and perturbations

$$\boldsymbol{\sigma} = -P_0\mathbf{1} + (\boldsymbol{u}\cdot\boldsymbol{\nabla}P_0)\,\mathbf{1} + \boldsymbol{\tau} \tag{2.3}$$

$$\phi = \phi_0 + \phi_1 \tag{2.4}$$

$$\rho = \rho_0 + \rho_1 \tag{2.5}$$

where P_0 is the initial hydrostatic presurre, $\boldsymbol{u}$ is the displacement vector, and $\boldsymbol{\tau}$ is the stress tensor for which the onstitutive equation of viscoelasticity holds. The second term on the right of (2.3) is required in order that the correct boundary condition is satisfied (Wolf, 1985). The potential perturbation ϕ_1 is the externally applied potential ϕ_2 plus the perturbation due to internal mass redistribution ϕ_3. The density perturbation ρ_1 is obtained from the continuity equation

$$\rho_1 = -\boldsymbol{\nabla}\cdot(\rho_0\boldsymbol{u})\,. \tag{2.6}$$

In spherical coordinates, the equation of motion and Poisson's equation in the initial state are

$$0 = -\rho_0 g_0\mathbf{e}_r - \boldsymbol{\nabla}P_0 \tag{2.7}$$

$$\boldsymbol{\nabla}^2\phi_0 = 4\pi G\rho_0 \tag{2.8}$$

where $\mathbf{e}_r$ is the unit vector in the radial direction and g_0 is the gravitational acceleration ($\boldsymbol{\nabla}\phi_0 = g_0\mathbf{e}_r$). The equation of motion and Poisson's equation in the perturbed state are

$$0 = -\rho_0\boldsymbol{\nabla}\phi_1 + \boldsymbol{\nabla}\cdot(\rho_0\boldsymbol{u})\,g_0\mathbf{e}_r - \boldsymbol{\nabla}\left(\boldsymbol{u}\cdot\rho_0 g_0\mathbf{e}_r\right) + \boldsymbol{\nabla}\cdot\boldsymbol{\tau} \tag{2.9}$$

$$\boldsymbol{\nabla}^2\phi_1 = -4\pi G\boldsymbol{\nabla}\cdot(\rho_0\boldsymbol{u}) \tag{2.10}$$

in which only first-oder terms enter.

We consider a Maxwell viscoelastic body. In Cartesian coordinate, the constitutive equation is

$$\partial_t\tau_{ij} + \frac{\mu}{\eta}\left(\tau_{ij} - \frac{1}{3}\tau_{kk}\delta_{ij}\right) = \lambda\partial_t\epsilon_{kk}\delta_{ij} + 2\mu\partial_t\epsilon_{ij} \tag{2.11}$$

where ∂_t denotes the partial derivative with respect to time t, λ and μ are the Lame parameters, and η is the visocisy. The strain tensor ϵ_{ij} is defined by

$$\epsilon_{ij} = \frac{1}{2}\left(\frac{\partial u_i}{\partial x_j} + \frac{\partial u_j}{\partial x_i}\right). \tag{2.12}$$

The Laplace transform of a function $f(t)$ is defined by

$$\tilde{f}(s) = L[f(t)] = \int_0^\infty f(t)e^{-st}dt \tag{2.13}$$

where s is the Laplace transform variable. The Laplace transform of the time derivative of the function $f(t)$ is

$$L[\partial_t f(t)] = s\tilde{f}(s) - f(0). \tag{2.14}$$

Using Equations (2.13) and (2.14), the Laplace transform of the constitutive equation (2.11) becomes

$$s\tilde{\tau}_{ij} - \tau_{ij}(0) + \frac{\mu}{\eta}\left(\tilde{\tau}_{ij} - \frac{1}{3}\tilde{\tau}_{kk}\delta_{ij}\right) = \lambda s\tilde{\epsilon}_{kk}\delta_{ij} - \lambda\epsilon_{kk}(0) + 2\mu s\tilde{\epsilon}_{ij} - 2\mu\epsilon_{ij}(0). \tag{2.15}$$

This can be rewritten as

$$\tilde{\tau}_{ij} = \lambda(s)\tilde{\epsilon}_{kk}\delta_{ij} + 2\mu(s)\tilde{\epsilon}_{ij} \quad \text{for} \quad t > 0 \tag{2.16}$$

with the following condition

$$\tau_{ij} = \lambda\epsilon_{kk} + 2\mu\epsilon_{ij} \quad \text{at} \quad t = 0 \tag{2.17}$$

where

$$\lambda(s) = \frac{\lambda s + \frac{\mu}{\eta}K}{s + \frac{\mu}{\eta}}, \quad \mu(s) = \frac{\mu s}{s + \frac{\mu}{\eta}}, \quad K = \lambda + \frac{2}{3}\mu. \tag{2.18}$$

Equation (2.16) has the same form as the constitutive equation for a Hook elastic body (2.17). Also, the equation of motion (2.9) and Poisson's equation (2.10) for the viscoelastic body are equivalent to those for the elastic body. We thus solve the equivalent elastic problem with parameters (2.18) and will inverse the Laplace transform to obtain the viscoelastic solution.

We consider spherically symmetric Earth models, for which the toroidal and spheroidal motions decouple. For the problem of deformation due to a point mass load located on $\theta = 0$, the toroidal motion is zero. The spherical harmonic expnasiosons of $\boldsymbol{u}$ and ϕ_1 are

$$\boldsymbol{u}(r,\theta) = \sum_{n=0}^{\infty}\left[U_n(r)P_n(\cos\theta)\boldsymbol{e}_r + V_n(r)\frac{\partial}{\partial\theta}P_n(\cos\theta)\boldsymbol{e}_\theta\right] \tag{2.19}$$

$$\phi_1(r,\theta) = \sum_{n=0}^{\infty}\Phi_n(r)P_n(\cos\theta). \tag{2.20}$$

The radial and tangential components of the equation of motion (2.9) and the Poisson's equation (2.10) become the following set of three differential equations of second-order

$$\begin{aligned} 0 = {} & -\rho_0\dot{\Phi}_n + \rho_0 g_0\chi_n - \rho_0\frac{d}{dr}(g_0U_n) + \frac{d}{dr}(\lambda\chi_n + 2\mu\dot{U}_n) \\ & + \frac{\mu}{r^2}[4\dot{U}_n r - 4U_n + n(n+1)(-U_n - r\dot{V}_n + 3V_n)] \end{aligned} \tag{2.21}$$

$$\begin{aligned} 0 = {} & -\rho_0\Phi_n - \rho_0 g_0 U_n + \lambda\chi_n + r\frac{d}{dr}\left[\mu\left(\dot{V}_n - \frac{V_n}{r} + \frac{U_n}{r}\right)\right] \\ & + \frac{\mu}{r}[5U_n + 3r\dot{V}_n - V_n - 2n(n+1)V_n] \end{aligned} \tag{2.22}$$

$$\ddot{\Phi}_n + \frac{2}{r}\dot{\Phi}_n - \frac{n(n+1)}{r^2}\Phi_n = -4\pi G(\rho_0\chi_n + \dot{\rho}_0 U_n) \tag{2.23}$$

where the dots denote the differenciation with respect to r. χ_n is obtained from the spherical harmonic expantion of the volume change

$$\boldsymbol{\nabla}\cdot\boldsymbol{u} = \sum_{n=0}^{\infty}\chi_n(r)P_n(\cos\theta) \tag{2.24}$$

$$\chi_n = \dot{U}_n + \frac{2}{r}U_n - \frac{n(n+1)}{r}V_n. \tag{2.25}$$

It is useful to transform these three differential euqations of second-order into six differential equations of first-order. We therefore introduce the radial and tangential stresses and the potential stress

$$T_{r,n} = \lambda\chi_n + 2\mu\dot{U}_n \tag{2.26}$$

$$T_{\theta,n} = \mu\left(\dot{V}_n - \frac{1}{r}V_n + \frac{1}{r}U_n\right) \tag{2.27}$$

$$Q_n = \dot{\Phi}_n + \frac{(n+1)}{r}\Phi_n + 4\pi G\rho_0 U_n. \tag{2.28}$$

In terms of the vector $\boldsymbol{Y} = (U_n, V_n, T_{r,n}, T_{\theta,n}, \Phi_n, Q_n)^t$, Equations (2.21–2.23) and (2.26–2.28) can be written in the form

$$\frac{d\boldsymbol{Y}}{dr} = \mathbf{A}\boldsymbol{Y} \tag{2.29}$$

where

$$\mathbf{A} = \begin{bmatrix} -\frac{2\lambda}{r\beta} & \frac{n(n+1)}{r}\frac{\lambda}{\beta} & \frac{1}{\beta} & 0 & 0 & 0 \\ -\frac{1}{r} & \frac{1}{r} & 0 & \frac{1}{\mu} & 0 & 0 \\ \frac{4}{r}\left(\frac{\gamma}{r} - \rho_0 g_0\right) & \frac{-n(n+1)}{r}\left(\frac{2\gamma}{r} - \rho_0 g_0\right) & -\frac{4\mu}{r\beta} & \frac{n(n+1)}{r} & \frac{-\rho_0(n+1)}{r} & \rho_0 \\ \frac{1}{r}\left(\rho_0 g_0 - \frac{2\gamma}{r}\right) & -\frac{1}{r^2}\left[2\mu - n(n+1)(\gamma+\mu)\right] & \frac{-\lambda}{r\beta} & \frac{-3}{r} & \frac{\rho_0}{r} & 0 \\ -4\pi G\rho_0 & 0 & 0 & 0 & -\frac{(n+1)}{r} & 1 \\ -4\pi G\rho_0\frac{(n+1)}{r} & \frac{4\pi G\rho_0 n(n+1)}{r} & 0 & 0 & 0 & \frac{n-1}{r} \end{bmatrix} \tag{2.30}$$

with

$$\beta = \lambda + 2\mu, \quad \gamma = \mu\left(\frac{3\lambda + 2\mu}{\lambda + \mu}\right). \tag{2.31}$$

2.1.2 Boundary conditions

We include an inviscid core in which the rigidity is zero, $\mu = 0$. The tangential stress (2.27) becomes $T_{\theta,n} = 0$. The field equations (2.21–2.23) become

$$-\dot{\Phi}_n + g_0\chi_n - \frac{d}{dr}(g_0 U_n) + \frac{\dot{T}_{r,n}}{\rho_0} = 0 \tag{2.32}$$

$$-\Phi_n - g_0 U_n + \frac{T_{r,n}}{\rho_0} = 0 \tag{2.33}$$

$$\ddot{\Phi}_n + \frac{2}{r}\dot{\Phi}_n - \frac{n(n+1)}{r^2}\Phi_n = -\frac{4\pi G\dot{\rho}_0}{g_0}\Phi_n. \tag{2.34}$$

If the radial derivative of Equation (2.33) is subtracted from Equation (2.32), then we obtain

$$\left(\dot{\rho}_0 + \frac{\rho_0^2 g_0}{K}\right)\chi_n = 0. \tag{2.35}$$

We consider the case $\chi_n = 0$ (if the quantity in the bracket is zero, then the Adams-Williamson condition is required in the core). The radial stress (2.26) becomes $T_{rn} = 0$. Equations (2.32) and (2.33) reduce to the following equation

$$U_n = -\frac{\Phi_n}{g}. \tag{2.36}$$

This means that the radial displacemt coincides with the displacement of an equipotential surface. The six differential equations (2.29) reduce to two differential equations in the components of the vector $\boldsymbol{Y} = (\Phi_n, Q_n)^t$. From Equations (2.28) and (2.34), the matrix $\mathbf{A}$ correponding to Equation (2.30) becomes

$$\mathbf{A} = \begin{bmatrix} 4a\pi G\rho_0/g_0 - (n+1)/r & 1 \\ \frac{8\pi G\rho_0(n-1)}{g_0 r} & \frac{(n-1)}{r}\frac{4\pi G\rho_0}{g_0} \end{bmatrix}. \tag{2.37}$$

Around the Earth centre, the density is contant, $\dot{\rho}_0 = 0$. The Poisson equation (2.34) becomes the Lapace equation, and the solution must be regualr at $r = 0$. We thus obtain

$$\boldsymbol{Y} = \begin{bmatrix} \Phi_n \\ Q_n \end{bmatrix} = {}^1C \begin{bmatrix} r^n \\ 2(n-1)r^{n-1} \end{bmatrix} \tag{2.38}$$

where ${}^1C$ is a constatnt of intergration. Equation (2.38) is employed as a starting solution in the core. This starting solution is propagated to the core-mantle boundary (CMB) using Equation (2.37). The CMB is a free-slip baoundary, and the tangential displacement just above the CMB is treated as a constant ${}^2C$. If $\Phi_n(b^-)$ and $Q_n(b^-)$ are the solutions just below the CMB ($r = b$), then the solution just above the CMB is expressed as

$$\begin{bmatrix} U_n(b^+) \\ V_n(b^+) \\ T_{r,n}(b^+) \\ T_{\theta,n}(b^+) \\ \Phi_n(b^+) \\ Q_n(b^+) \end{bmatrix} = {}^1C \begin{bmatrix} -\Phi_n(b^-)/g(b) \\ 0 \\ 0 \\ 0 \\ \Phi_n(b^-) \\ Q_n(b^-) \end{bmatrix} + {}^2C \begin{bmatrix} 0 \\ 1 \\ 0 \\ 0 \\ 0 \\ 0 \end{bmatrix} + {}^3C \begin{bmatrix} 1 \\ 0 \\ \rho_0(b^-)g_0(b) \\ 0 \\ 0 \\ 4\pi G\rho_0(b^-) \end{bmatrix}. \tag{2.39}$$

The third constant ${}^3C$ is the discontinuity of the radial displacement at the CMB, and this means that the CMB boundary penetrates equipotential surfaces determined by Equation (2.36) (Chinnery, 1975). The three linearly independent vectors at the CMB (2.39) are propagated to the Earth surface using Equation (2.30). We write the three solutions at the Earth

surface ($r = a$) as

$$\begin{bmatrix} U_n(a,s) \\ V_n(a,s) \\ T_{r,n}(a,s) \\ T_{\theta,n}(a,s) \\ \Phi_n(a,s) \\ Q_n(a,s) \end{bmatrix} = {}^1C(s) \begin{bmatrix} {}^1U_n(a,s) \\ {}^1V_n(a,s) \\ {}^1T_{r,n}(a,s) \\ {}^1T_{\theta,n}(a,s) \\ {}^1\Phi_n(a,s) \\ {}^1Q_n(a,s) \end{bmatrix} + {}^2C(s) \begin{bmatrix} {}^2U_n(a,s) \\ {}^2V_n(a,s) \\ {}^2T_{r,n}(a,s) \\ {}^2T_{\theta,n}(a,s) \\ {}^2\Phi_n(a,s) \\ {}^2Q_n(a,s) \end{bmatrix} + {}^3C(s) \begin{bmatrix} {}^3U_n(a,s) \\ {}^3V_n(a,s) \\ {}^3T_{r,n}(a,s) \\ {}^3T_{\theta,n}(a,s) \\ {}^3\Phi_n(a,s) \\ {}^3Q_n(a,s) \end{bmatrix} \tag{2.40}$$

where we explicitly write the dependence on the Laplace transform variable s.

The three constans ${}^1C$, ${}^2C$, and ${}^3C$ are determined by the surface boundary conditions for $T_{r,n}(a,s)$, $T_{\theta,n}(a,s)$, and $Q_n(a,s)$. We consider a surface point load of unit mass located on $\theta = 0$. The spherical harmonic expnasioson of the surface density γ is (Longman, 1962)

$$\gamma = \sum_{n=0}^{\infty} \Gamma_n P_n(\cos\theta) \quad \text{where} \quad \Gamma_n = \frac{2n+1}{4\pi a^2}. \tag{2.41}$$

It excerts the radial stress, $T_{r,n}(a) = -g_0(a)\Gamma_n$. The tangential stress is zero, $T_{\theta,n}(a) = 0$. In addition, the load produces a potential inside the Earth

$$\phi_2 = \sum_{n=0}^{\infty} \Phi_{2,n}(r) P_n(\cos\theta) \quad \text{where} \quad \Phi_{2,n}(r) = \Phi_{2,n}(a)\left(\frac{r}{a}\right)^n = -\frac{4\pi a G \Gamma_n}{2n+1}\left(\frac{r}{a}\right)^n \tag{2.42}$$

Let $\Phi_{3,n}(r)$ be the spherical harmonic coefficient of the potential perturbation due to internal mass redistribution ϕ_3. Outside the Earth

$$\Phi_{3,n}(r) = \Phi_{3,n}(a)\left(\frac{r}{a}\right)^{-n-1}. \tag{2.43}$$

The required conditions across the surface are

$$\Phi_{2,n}(a^-) = \Phi_{2,n}(a^+) \tag{2.44}$$

$$\Phi_{3,n}(a^-) = \Phi_{3,n}(a^+) \tag{2.45}$$

$$\dot{\Phi}_{3,n}(r)\Big|_{r=a^-} + 4\pi G\rho_0 U_n(a^-) = \dot{\Phi}_{3,n}(r)\Big|_{r=a^+} \tag{2.46}$$

The potential stress (2.28) just below the surface is

$$Q_n(a^-) = \dot{\Phi}_{2,n}(r)\Big|_{r=a^-} + \frac{(n+1)}{a}\Phi_{2,n}(a^-) + \dot{\Phi}_{3,n}(r)\Big|_{r=a^-} + \frac{(n+1)}{a}\Phi_{3,n}(a^-) + 4\pi G\rho_0(a^-)U_n(a^-) \tag{2.47}$$

Using Equations (2.42–2.46), we have

$$Q_n(a^-) = \frac{2n+1}{a}\Phi_{2,n}(a^-). \tag{2.48}$$

If we define $\boldsymbol{b} = [T_{r,n}(a,s), T_{\theta,n}(a,s), Q_n(a,s)]^t$, then the boundary conditions are

$$\boldsymbol{b} = \begin{bmatrix} -g_0(a)\Gamma_n \\ 0 \\ \frac{2n+1}{a}\Phi_{2,n}(a) \end{bmatrix} \tag{2.49}$$

If we define $\boldsymbol{C}(s) = \left[{}^1C(s), {}^2C(s), {}^3C(s)\right]^t$, then

$$\boldsymbol{C}(s) = \frac{\mathbf{M}^*(s)}{\det \mathbf{M}(s)}\boldsymbol{b} \quad \text{where} \quad \mathbf{M}(s) = \begin{bmatrix} {}^1T_{r,n}(a,s) & {}^2T_{r,n}(a,s) & {}^3T_{r,n}(a,s) \\ {}^1T_{\theta,n}(a,s) & {}^2T_{\theta,n}(a,s) & {}^3T_{\theta,n}(a,s) \\ {}^1Q_n(a,s) & {}^2Q_n(a,s) & {}^3Q_n(a,s) \end{bmatrix} \tag{2.50}$$

where $\mathbf{M}^*$ is the transpose matrix of the cofactors. If we define $\boldsymbol{Y}(s) = [U_n(a,s), V_n(a,s), \Phi_n(a,s)]^t$, then

$$\boldsymbol{Y}(s) = \mathbf{N}(s)\frac{\mathbf{M}^*(s)}{\det \mathbf{M}(s)}\boldsymbol{b} \quad \text{where} \quad \mathbf{N}(s) = \begin{bmatrix} {}^1U_n(a,s) & {}^2U_n(a,s) & {}^3U_n(a,s) \\ {}^1V_n(a,s) & {}^2V_n(a,s) & {}^3V_n(a,s) \\ {}^1\Phi_n(a,s) & {}^2\Phi_n(a,s) & {}^3\Phi_n(a,s) \end{bmatrix}. \tag{2.51}$$

If we denote the zeros of $\det \mathbf{M}(s)$ as s_j (for $j = 1, \cdots, N$) and assume that they are simple poles, the application of Cauchy's residue theorem yields

$$\boldsymbol{Y}(t) = \boldsymbol{Y}^E\delta(t) + \sum_{j=1}^{N} \frac{\mathbf{N}(s_j)\mathbf{M}^*(s_j)\boldsymbol{b}}{\frac{d}{ds}\left[\det \mathbf{M}(s)\right]|_{s=s_j}} e^{s_j t} \tag{2.52}$$

where $\delta(t)$ is the Dirac delta function and

$$\boldsymbol{Y}^E = \lim_{s\to\infty} \boldsymbol{Y}(s). \tag{2.53}$$

The elastic component $\boldsymbol{Y}^E\delta(t)$ is added in order to satisfy the condition (2.17). Using these solutions, Love numbers are defined by

$$\begin{bmatrix} U_n(a,t) \\ V_n(a,t) \\ \Phi_{3,n}(a,t) \end{bmatrix} = \Phi_{2,n}(a) \begin{bmatrix} h_n(a,t)/g_0(a) \\ l_n(a,t)/g_0(a) \\ k_n(a,t) \end{bmatrix}. \tag{2.54}$$

Using Equations (2.52) and (2.54), we obtain

$$k_n(t) = k_n^E \delta(t) + \sum_{j=1}^{N} \beta_{n,j} e^{s_{n,j} t} \tag{2.55}$$

$$h_n(t) = h_n^E \delta(t) + \sum_{j=1}^{N} \gamma_{n,j} e^{s_{n,j} t} \tag{2.56}$$

where N is the number of eigenmode, s_j is the inverse relaxation time of eigenmode j, and β_j and γ_j are strengths of eigenmode j. The relative strengths of eigenmode j for both Love numbers are given by $\frac{\gamma_j}{s_j} / \sum_{j=1}^{N} \frac{\beta_j}{s_j}$ and $\frac{\gamma_j}{s_j} / \sum_{j=1}^{N} \frac{\gamma_j}{s_j}$.

2.2 Earth rotation variation

This section explains the linearized Liouville equation which is usually used for the Earth rotation variation in ice age problems. The formulation follows that of Nakada (2009), Mitrovica & Wahr (2011), and Chapter 3 of Sabadini et al. (2016).

2.2.1 Fundamental equation

If we assume that no external torques act on the system, then in an Earth fixed refrence frame, Euler's equation (or Liouville's equation) becomes

$$\frac{d\boldsymbol{H}(t)}{dt} + \boldsymbol{\omega}(t) \times \boldsymbol{H}(t) = 0 \tag{2.57}$$

where $\boldsymbol{H}$ is the angular momentum and $\boldsymbol{\omega}$ is the angular velocity. Using the inertia tensor $\mathbf{I}$, $\boldsymbol{H}$ is given by $\boldsymbol{H} = \mathbf{I} \cdot \boldsymbol{\omega}$. The term $d\boldsymbol{H}(t)/dt$ is safely neglected in evaluating the secular variations due to the GIA process (Nakada, 2009). The angular velocity and the inertia tensor are decomposed into initial states and perturbations

$$\boldsymbol{\omega}(t) = \begin{bmatrix} 0 \\ 0 \\ 1 \end{bmatrix} \Omega + \begin{bmatrix} m_1(t) \\ m_2(t) \\ m_3(t) \end{bmatrix} \Omega \tag{2.58}$$

$$\mathbf{I}(t) = \begin{bmatrix} A & 0 & 0 \\ 0 & A & 0 \\ 0 & 0 & C \end{bmatrix} + \begin{bmatrix} \Delta I_{11}(t) & \Delta I_{21}(t) & \Delta I_{31}(t) \\ \Delta I_{12}(t) & \Delta I_{22}(t) & \Delta I_{32}(t) \\ \Delta I_{13}(t) & \Delta I_{23}(t) & \Delta I_{33}(t) \end{bmatrix} \tag{2.59}$$

where Ω is the mean angular velocity of the Earth and A and C are the equatorial and polar moments of inertia for a hydrostatic equilibrium state of the Earth (see Section 2.2.2). By putting Equations (2.58) and (2.59) into Equation (2.57) and neglecting second order terms, we obtain

$$m_1(t) = \frac{\Delta I_{13}(t)}{C - A} \tag{2.60}$$

$$m_2(t) = \frac{\Delta I_{23}(t)}{C - A} \tag{2.61}$$

$$m_3(t) = -\frac{\Delta I_{33}(t)}{C}. \tag{2.62}$$

The change in the orientation of the rotational axis, $m_1(t)$ and $m_2(t)$, is termed as true polar wander (TPW).

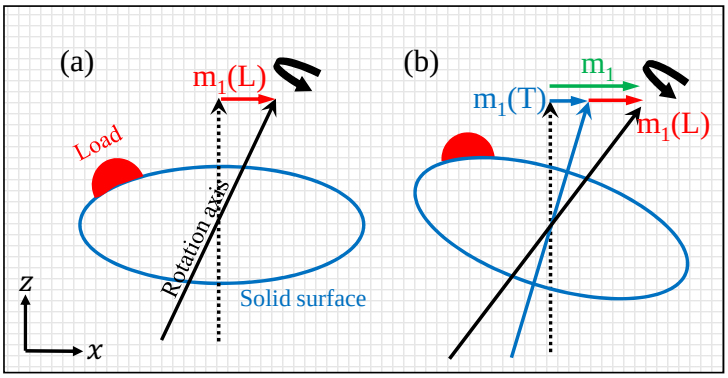

Figure 2.1. Schematic illustrations of GIA-induced true polar wander.

The inertia tensor perturbation, which will be derived in Section 2.2.2, is

$$\Delta I_{ij}(t) = \frac{a^5}{3G} k_2^T(t) * \left[\omega_i(t)\omega_j(t) - \frac{1}{3}\omega^2(t)\delta_{ij}\right] + I_{ij}^L(t) + k_2^L(t) * I_{ij}^L(t) \tag{2.63}$$

where k_2^T and k_2^L are tidal and load Love numbers. The first term is due to the inertia tensor perturbation driven by changes in the centrifugal potential (Figure 2.1b). The second and third terms are the inertia tensor perturbation due to the surface load and load induced deformation (Figure 2.1a). Using Equation (2.63), the linearized Liuville's equations (2.60)–(2.62)

become

$$m_1(t) = \frac{a^5\Omega^2}{3G\,(C-A)} k_2^T(t) * m_1(t) + \frac{1}{C-A}\left[I_{13}^L(t) + k_2^L(t) * I_{13}^L(t)\right] \tag{2.64}$$

$$m_2(t) = \frac{a^5\Omega^2}{3G\,(C-A)} k_2^T(t) * m_2(t) + \frac{1}{C-A}\left[I_{23}^L(t) + k_2^L(t) * I_{23}^L(t)\right] \tag{2.65}$$

$$m_3(t) = -\frac{1}{C}\left[I_{33}^L(t) + k_2^L(t) * I_{33}^L(t)\right]. \tag{2.66}$$

2.2.2 MacCullagh's formula and inertia tensor

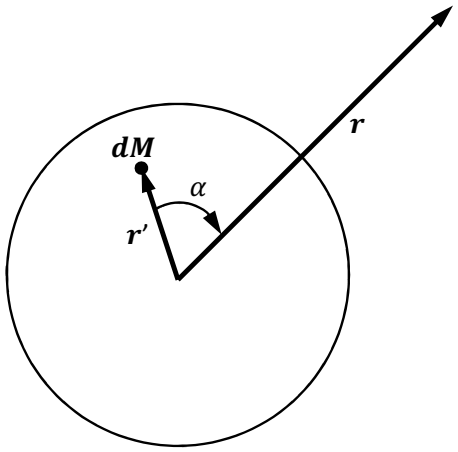

Figure 2.2. Geometry involved in the integration of graviational potential. $\boldsymbol{r}_i$ is the radius vector to the mass dM from the centre of mass. $\boldsymbol{r}$ is the corresponding radius vector to the unit point mass.

First we derive MacCullagh's formula following Section 5.8 of Goldstein (1980). Consider the geometry in Figure 2.2. The integration of the gravitational potential at $\boldsymbol{r}$ due to the mass element dM is expaded as

$$\phi = -\frac{G}{r}\int \sum_{n=0}^{\infty}\left(\frac{r'}{r}\right)^n P_n(\cos\alpha)\, dM. \tag{2.67}$$

The term for $n = 2$ can be written in dyadic form

$$\phi_{n=2} = \frac{G}{2r^5}\int \boldsymbol{r}\cdot\left(r'^2\mathbf{1} - 3\boldsymbol{r}'\otimes\boldsymbol{r}'\right)\cdot\boldsymbol{r}dM \tag{2.68}$$

where $\otimes$ denotes the dyadic product (or the tensor product). On the other hand, the inertia tensor of the body can be written in dyadic form

$$\mathbf{I} = \int \left(r'^2 \mathbf{1} - \boldsymbol{r}' \otimes \boldsymbol{r}' \right) dM, \tag{2.69}$$

and the trace of the inertia tensor is

$$\mathrm{Tr}\mathbf{I} = 2 \int r'^2 dM. \tag{2.70}$$

Using Equations (2.69) and (2.70), Equation (2.68) becomes

$$\phi_{n=2} = \frac{G}{2r^5} \boldsymbol{r} \cdot \left[(-\mathrm{Tr}\mathbf{I})\, \mathbf{1} + 3\mathbf{I} \right] \cdot \boldsymbol{r}. \tag{2.71}$$

This is known as MacCullagh's formula.

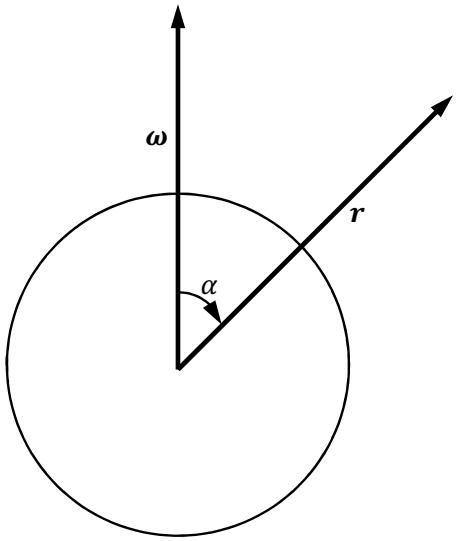

Figure 2.3. Geometry involved in centrifugal potential.

Next we derive the inertia tensor perturbation driven by changes in the centrifugal potential. Consider the geometry in Figure 2.3 . The centrifugal potential at $\boldsymbol{r}$ is

$$\phi^R(t) = -\frac{1}{3}\omega^2(t) r^2 + \frac{1}{6}\omega^2(t) r^2 P_2(\cos\alpha) \tag{2.72}$$

Similar to (2.68), the second term can be written in dyadic form

$$\phi^R_{n=2}(t) = -\frac{1}{6}\boldsymbol{r}\cdot\left[\omega^2(t)\mathbf{1} - 3\boldsymbol{\omega}(t)\otimes\boldsymbol{\omega}(t)\right]\cdot\boldsymbol{r}. \tag{2.73}$$

The degree-2 potential purturbation at the Earth surface($r = a$) due to internal mass redistribution driven by changes in the centrifugal potential is $k_2^T(t) * \Lambda_{n=2}(t)$ where $r = a$ in $\Lambda_{n=2}(t)$ and $*$ denotes a time convolution. Substituting it into the MacCullagh's formula (2.71) for $r = a$,

$$k_2^T(t) * \left\{-\frac{1}{6}\left[\omega^2(t)\mathbf{1} - 3\boldsymbol{\omega}(t)\otimes\boldsymbol{\omega}(t)\right]\right\} = \frac{3G}{2a^5}\left\{\left[-\frac{1}{3}\mathrm{Tr}\mathbf{I}(t)\right]\mathbf{1} + \mathbf{I}(t)\right\} \tag{2.74}$$

and we obtain

$$\mathbf{I}(t) = \mathbf{I}^{NR} + \frac{a^5}{3G}k_2^T(t) * \left[\boldsymbol{\omega}(t)\otimes\boldsymbol{\omega}(t) - \frac{1}{3}\omega^2(t)\mathbf{1}\right] \tag{2.75}$$

where $\mathbf{I}^{NR} = \frac{1}{3}\mathrm{Tr}\mathbf{I}(t)$ is the inertia tensor of the Earth in the absence of rotational defromation (see Munk & Macdonald, 1960, p25).

If we assume that the Earth is in hydrostatic equilibrium state with the constant angular velocity $\boldsymbol{\omega} = (0, 0, \Omega)$, then the equilibrium polar and equatorial inertia moments are given by

$$\begin{pmatrix} A & 0 & 0 \\ 0 & A & 0 \\ 0 & 0 & C \end{pmatrix} = \mathbf{I}^{NR} + \frac{a^5}{3G}\begin{pmatrix} -\frac{1}{3}\Omega^2 & 0 & 0 \\ 0 & -\frac{1}{3}\Omega^2 & 0 \\ 0 & 0 & \frac{2}{3}\Omega^2 \end{pmatrix}\lim_{t\to\infty} k_2^T(t) * H(t) \tag{2.76}$$

where $H(t)$ is a Heavisde step function.

Finaly we derive the inertia tensor perturbation due to load induced deformation. Let the surface load $L(\theta, \psi, t)$, where θ and ψ are the colatitude and longitude, represent the redistribution of ice and water (the details will be described in Section 2.3). The inertia tensor perturbation due to the surface load is

$$\mathbf{I}^L(t) = \int_s L(\theta', \psi', t)\left(a^2\mathbf{1} - \boldsymbol{r}'\otimes\boldsymbol{r}'\right)ds \tag{2.77}$$

where ds is the element of are on the Earth's surface.

Similar to (2.71), the gravitational potential at $\boldsymbol{r}$ due to the surface load is

$$\phi^L_{n=2}(t) = \frac{3G}{2r^5}\boldsymbol{r}\cdot\mathbf{I}^L(t)\cdot\boldsymbol{r} \tag{2.78}$$

where $\mathrm{Tr}\mathbf{I}^L(t) = 0$ if we assume that the total mass of ice and water is conserved. The degree-2 potential purturbation at the Earth surface due to internal mass redistribution driven by surface loading is $k^L_2(t) * \phi^L_{n=2}(t)$ where $r = a$ in $\phi^L_{n=2}(t)$. Substituiting it into the MacCullagh's formula (2.71) for $r = a$, we obtain

$$\mathbf{I}(t) = \mathbf{I}^{NR} + k^L_2(t) * \mathbf{I}^L(t). \tag{2.79}$$

The second term is the inertia tensor perturbation due to load induced deformation.

2.3 Sea level change

This section explains the "sea level equation" which describe sea level change due to GIA (Farrell & Clarck 1976; Milne & Mitrovica 1998). The ocean surface is constrained to remain an equipotential surface of gravitational field (geoid). Sea level is defined as height of geoid relative to height of solid Earth surface.

2.3.1 Sea level change due to surface load

First we derive sea level change due to the surface point mass. Consider the geometry in Fig (2.4). The graviational potential at the surface due to the point mass is expanded as

$$\phi^L(\alpha, t) = \sum_{n=0}^{\infty}\frac{GM_P(t)}{a}P_n(\cos\alpha) \tag{2.80}$$

Using the load Love numbers k^L_n and h^L_n defined by Equation (2.54), sea level change due to the point mass is given by

$$S^P(\alpha, t) = \frac{\phi^L(\alpha, t)}{g_0} + \frac{1}{g_0}\sum_{n=0}^{\infty}\frac{GM_P(t)}{a} * k^L_n(t)P_n(\cos\alpha) - \sum_{n=0}^{\infty}\frac{GM_P(t)}{a} * \frac{h^L_n(t)}{g_0}P_n(\cos\alpha) \tag{2.81}$$

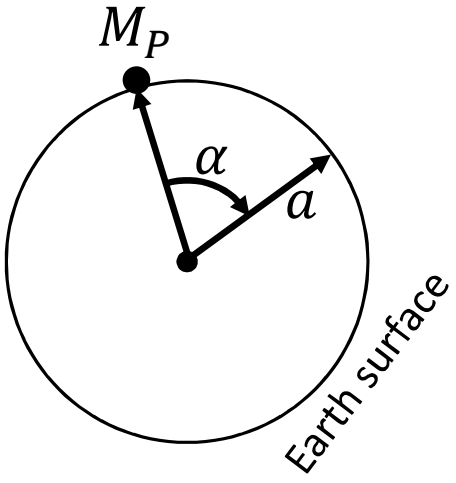

Figure 2.4. Geometry involved in gravitational potential due to a point mass.

where g_0 is the gravitational acceralation at the Earth surface. The first term is the geoid perturbation due to the point mass. The second term is the geoid perturbation due to internal mass redistribution. The third term is the minus of the radial displacement of the solid surface. Writting $g_0 = GM_E/a^2$ where M_E is the Earth's mass, Equation (2.81) can be rewritten as

$$S^P(\alpha, t) = \frac{a}{M_E} \sum_{n=0}^{\infty} M_P(t) * \left[\delta(t) + k_n^L(t) - h_n^L(t)\right] P_n(\cos\alpha). \tag{2.82}$$

Next we derive sea level change due to surface load redistribution. The surface load, $L(\theta, \psi, t)$, where θ and ψ are respectively the colatitude and longitude, can be written as

$$L(\theta, \psi, t) = \rho_I I(\theta, \psi, t) + \rho_W W(\theta, \psi, t) \tag{2.83}$$

where ρ_i and ρ_W are the density of ice and sea water and I and W are changes in ice and water thichness. Consider the geometry in Fig (2.5). The sea level change due to surface load redistribution is given by the convolution integral

$$S^L(\theta, \psi, t) = \int_s \frac{a}{M_E} \sum_{n=0}^{\infty} L(\theta', \psi', t) * \left[\delta(t) + k_n^L(t) - h_n^L(t)\right] P_n(\cos\alpha) ds \tag{2.84}$$

where ds is the element of area on the surface.

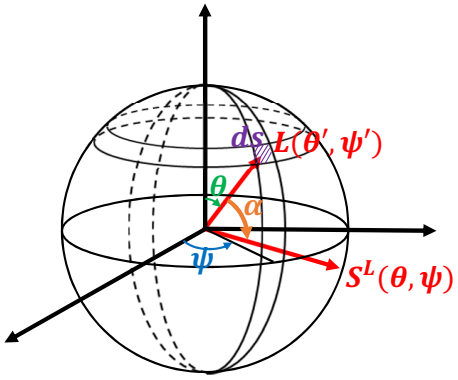

Figure 2.5. Geometry involved in gravitational potential due to a surface mass.

2.3.2 Sea level change due to Earth rotation

Using Equations (2.58) and (2.72), we obtain the following expression for the degree-2 perturbation to the centrifugal potential from equilibrium value (Millne & Mitrovica 1998)

$$\Lambda(\theta,\psi,t) = \sum_{m=0}^{2}\left[\Lambda_{2m}^{C}(t)\cos m\psi + \Lambda_{2m}^{S}(t)\sin m\psi\right] P_{2m}(\cos\theta) \tag{2.85}$$

where

$$\begin{aligned}
\Lambda_{20}^{C}(t) &= \frac{a^2\Omega^2}{6\sqrt{5}}\left[m_1^2(t) + m_2^2(t) - 2m_3^2(t) - 4m_3(t)\right] P_{20}\\
\Lambda_{21}^{C}(t) &= -\frac{a^2\Omega^2}{\sqrt{15}} m_1(t)\left[1 + m_3(t)\right]\cos\psi P_{21}\\
\Lambda_{21}^{S}(t) &= -\frac{a^2\Omega^2}{\sqrt{15}} m_2(t)\left[1 + m_3(t)\right]\sin\psi P_{21}\\
\Lambda_{22}^{C}(t) &= -\frac{a^2\Omega^2}{2\sqrt{15}}\left[m_1^2(t) - m_2^2(t)\right]\cos 2\psi P_{22}\\
\Lambda_{22}^{S}(t) &= -\frac{a^2\Omega^2}{\sqrt{15}} m_1(t)m_2(t)\sin 2\psi P_{22}.
\end{aligned} \tag{2.86}$$

Similar to Equation (2.81), the sea level change due to the perturbation in the centrifugal potential is given by

$$S^{R}(\theta,\psi,t) = \frac{1}{g_0}\left[\Lambda(\theta,\psi,t) + \Lambda(\theta,\psi,t) * k_2^{T}(t) - \Lambda(\theta,\psi,t) * h_2^{T}(t)\right]. \tag{2.87}$$

2.3.3 Mass conservation

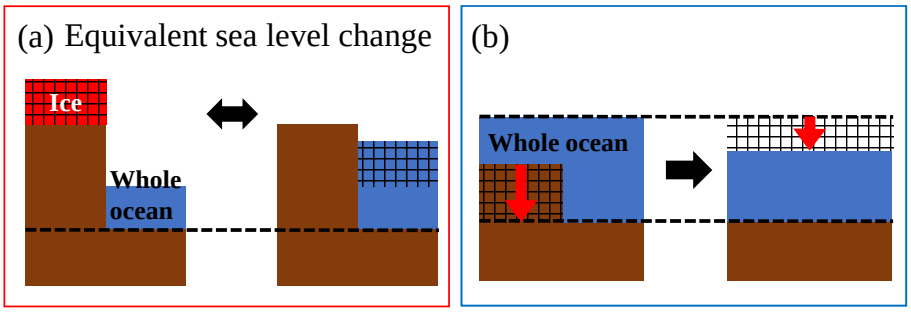

Figure 2.6. Schematic illustrations of sea level components associated with mass conservation.

The sea level equation is given by

$$S(\theta, \psi, t) = S^L(\theta, \psi, t) + S^R(\theta, \psi, t) + c(t). \tag{2.88}$$

$c(t)$ is a globaly uniform shift in sea level which is determined to satisfy the mass conservation

$$M_I(t) + M_W(t) = 0 \tag{2.89}$$

where $M_I(t)$ and $M_W(t)$ are changes in ice and water mass, respectively. We obtain

$$c(t) = -\frac{M_I(t)}{\rho_W A_O(t)} - \left\langle S^L(\theta, \psi, t) + S^R(\theta, \psi, t) \right\rangle_O \tag{2.90}$$

where $A_O(t)$ is ocean area and $<>_O$ means average over ocean area. The first term is the equivalent sea level change (Figure 2.6a). Figure 2.6b shows the contribution of the second term, which is termed syphoning (Mitrovica & Milne, 2002).

Equation (2.88) is an integral equation because the sea level change appears on the right-hand side through water thickness change. The equation is solved iteratively by successively refining an initial approximation to the sea level change.

Chapter 3

Non-monotonic post-deglacial relative sea level changes at the aftermath of the Marinoan snowball Earth meltdown

3.1 Introduction

The Earth system, including its hydrosphere, atmosphere, and biosphere, must have experienced dramatic transformations to a new steady state after a large perturbation such as a snowball Earth global glaciation. One such Earth system response is the large magnitude relative sea level (RSL) change that occurred in association with a snowball episode (Hoffman, 2011). The Marinoan snowball Earth, which ended at ~635 Ma, offers us the best sedimentary and geochemical records for studying the RSL history of Earth system response to such a large perturbation and its accompanied changes in the atmosphere and biosphere.

RSL changes in the aftermath of Marinoan snowball meltdown have been inferred from the deposition of cap dolostones (Hoffman et al., 2007), and a 1–1.5 km eustatic sea level (ESL) rise for the Marinoan deglaciation was estimated from the Otavi Group sediment of Namibia

(Hoffman, 2011). Hoffman and Macdonald (2010) examined the depositional environments of cap dolostones for the Congo and Kalahari cratons in Namibia and inferred a sequence of transgression, regression, and transgression during the melting phase, referred to as the syn-deglacial phase here (see Figure 3.1b). They proposed that both transgression phases are due to ice sheet melting, and that the regression interrupting the transgressive cap dolostone sequence is caused by the loss of gravitational attraction between ice sheet and seawater, as analogous to the RSL change in Greenland from the last deglaciation in the Late Pleistocene (Clark, 1976). The regression is inferred from the presence of deeper water turbidites at the base of the lower-slope sections associated with the Otavi bank (Hoffman et al., 2007), and from the interpretation of the formation of sheet cracks near the base of the cap dolostones on the margins of the Congo and Kalahari cratons (Hoffman & Macdonald, 2010). Zhou et al. (2010) inferred a sequence of transgression, regression and transgression based on the stratigraphic studies of cap dolostones in South China. They proposed that the first transgression is due to a rapid ice sheet melting in the syn-deglacial phase. However, they interpreted the karst-like dissolution features at the top of the cap dolostones as a brief disruption or hiatus in carbonate sedimentation, possibly a brief time window of RSL drop when the rate of isostatic rebound exceeded that of the general transgression. The subsequent growth of crystal fans of barite, or in some cases perhaps aragonite, occurring in the inner surface of cavities or outer surface of boulders or breccia in some topographically high areas marks a second transgression at a time after the complete glacial meltdown, referred to as the post-deglacial phase here.

Predictions for RSL changes due to glacial isostatic adjustment (GIA) associated with a snowball Earth would be crucial in interpreting the sedimentary-inferred RSL changes such as those in Congo/Kalahari and South China cratons. Liu and Peltier (2013) examined the RSL changes due to snowball glaciation based on the model with a 570 Ma continental configuration, a flat land surface and ocean bottom, and a ~1000 m ESL change. They estimated the RSL drop along continental coastlines at equilibrium state during the snowball period and concluded that the predicted elevations of the land surface above the ocean surface are

broadly consistent with the estimate of the depth difference between a carbonate platform and its lower-slope from the Otavi Group sediment of Namibia.

Creveling and Mitrovica (2014) were the first to examine the spatial and temporal patterns of GIA-based RSL changes due to Marinoan snowball deglaciation. They adopted a 635 Ma paleogeographic reconstruction and topography consistent with mean values in modern topography. Their results show that: (i) the predicted RSL changes exhibit significant geographic variability, including a syn-deglacial RSL drop or stillstand at some sites, and (ii) that sea level continues to rise in the post-deglacial phase in some areas and thus the timescale for transgressive cap dolostone deposition needs not to be confined to the syn-deglacial phase. It is instructive that the variability in their sea level histories encompasses the range of variability in sedimentary-inferred RSL changes for specific geologic sites. However, their results did not include non-monotonic RSL behavior in the post-deglacial phase characterized by an RSL drop and a resumed transgression, such as that inferred in South China. We note that such a non-monotonic RSL behavior is not expected in the post-deglacial phase for the last deglaciation (e.g. Tushingham & Peltier, 1991). The post-deglacial phase of the Last Glacial Maximum (LGM) that peaked at ~21 kyr ago was of duration ~10 kyr (e.g. Lambeck et al., 2014). That is, non-monotonic RSL behavior arises from a significantly longer post-deglacial GIA-response than that for the last deglaciation, and may be a diagnostic GIA-signal for Marinoan snowball deglaciation.

Here we evaluate RSL changes associated with Marinoan snowball deglaciation by considering the effects of time-dependent shoreline migration and ocean bathymetry (Milne et al., 1999; Lambeck et al., 2003) and their uncertainties, as well as Earth's rotation (Milne & Mitrovica, 1996; Mitrovica et al., 2005). We must also consider paleotopography describing the location of paleo-shorelines and paleo-water depths when we discuss the RSL change inferred from sedimentary records. Our focus here will be to examine post-deglacial RSL change characterized by an RSL drop and a resumed transgression such as those in South China, and this history may also be sensitive to mantle viscosity structure. Moreover, the results may help to constrain the rate of an expectedly drastic evolution of the Earth system

in the aftermath of a snowball state, for example, the duration of the syn-deglaciation, the duration of cap dolostone deposition, and the recovery rate of the biosphere. All are closely linked to a global rate of weathering, organic burial, changing ocean chemistry, the rise of atmospheric O_2 and fall of atmospheric CO_2 concentrations (Bao et al., 2008; Cao & Bao, 2013). Thus, our modeling study can offer an independent test on the timing and duration of the Marinoan ^{17}O depletion (MOSD) event as recorded in basal Ediacaran sedimentary rocks world-wide.

The paper is organized as follows. In Section 3.2, we describe the viscosity and ice models, as well as models for continental distribution, topography, and ocean bathymetry. In Section 3.3, we examine the syn- and post-deglacial RSL changes by considering the impacts of coastline geometry, syn-deglacial duration and mantle viscosity on the syn- and post-deglacial RSL drops. In Section 3.4, we compare sedimentary-inferred and predicted RSL changes and try to establish some constraints on the syn-deglacial duration, mantle viscosity and the duration of the MOSD. The results obtained in this study are summarized in Section 3.5.

3.2 Model descriptions

The numerical method adopted here follows Nakada et al. (2016). Briefly, solving the sea level equation for the GIA processes (Farrell & Clark, 1976) requires an input of viscoelastic Earth structure, geography/topography and ice sheet models. We use the seismological Preliminary Reference Earth Model (PREM, Dziewonski & Anderson, 1981) for density and elastic constants. We adopt two types of rheological model (see Figure 1.3). One is a simple three-layer viscosity model characterized by elastic lithospheric thickness (H), upper mantle viscosity (η_{um}) and lower mantle viscosity (η_{lm}). The adopted values for H, η_{um}, and η_{lm} are: H = 65, 100 and 200 km, η_{um} = (2, 4, 7) $\times$ 10^{20} Pa s and η_{lm} = (5, 10, 50) $\times$ 10^{21} Pa s. Lambeck et al. (2014) indicated a typical value of 2×10^{20} Pa s for the oceanic upper mantle viscosity from analyses of far-field ocean islands and continental margin RSL data largely influenced by isostatic response due to the oceanic upper mantle viscosity. Lambeck et al. (2017) have also inferred an average continental upper mantle viscosity of (3.5 – 7.5) $\times$ 10^{20}

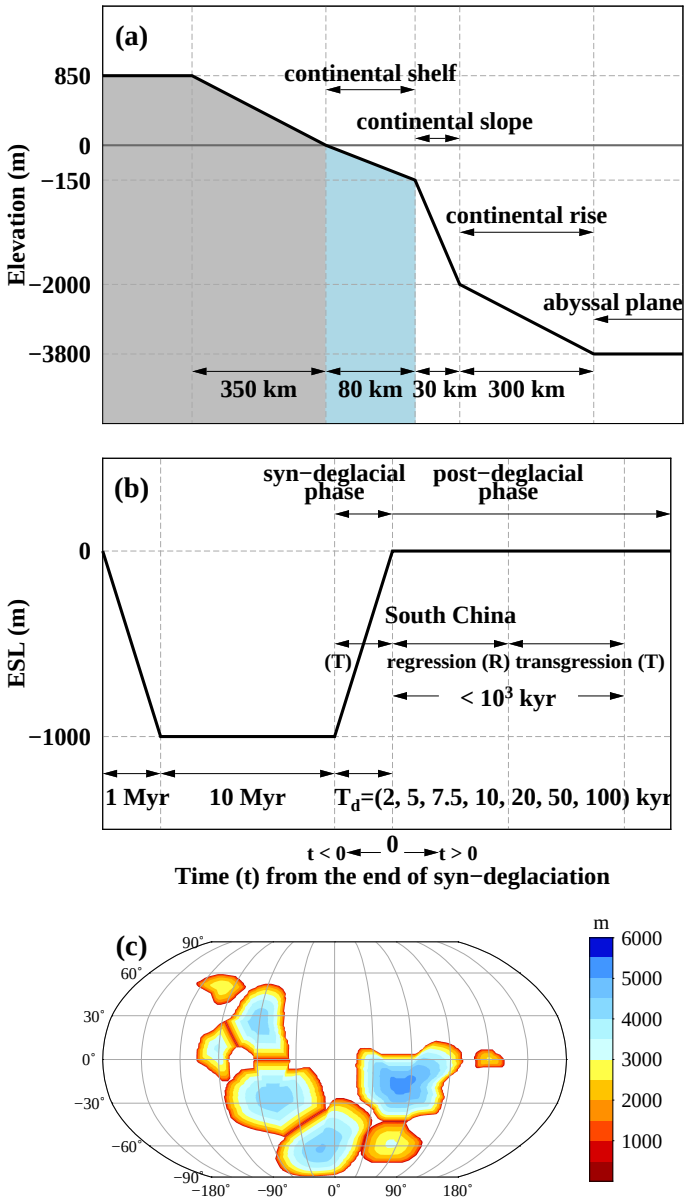

Figure 3.1. (a) Schematic figure for the cross section of the assumed topography of the solid Earth surface at the reference time (initial topography prior to Marinoan snowball glaciation). (b) Schematic ESL histories illustrating syn-deglacial phase with a duration T_d and post-deglacial phase ($t > 0$), and the approximate time of the transgressions (T) and the interrupting regression (R) in South China. The duration of the regression and transgression in the post-deglacial phase is based on the reference time adopted in this study (1 Myr). (c) Grounded ice thickness distribution at the maximum glaciation.

Pa s and effective lithospheric thickness of (85 – 120) km from GIA-related geological and geophysical data in the glaciated region for the North American Late Wisconsin ice sheet. The values of H = 65 km and $\eta_{um} = 4 \times 10^{20}$ Pa s are the same as those inferred from the observed RSL changes due to the melting of British and Scandinavian ice sheets (Lambeck & Johnston, 1998). The upper mantle viscosity of 4×10^{20} Pa s may be an average value for the above references (e.g. Nakada & Lambeck, 1991; Lambeck et al., 2017). The lower mantle viscosity of 5×10^{21} Pa s may be a lower bound as inferred from the Holocene sea level observations in the Australian region (Nakada & Lambeck, 1989) and joint inversion using GIA and convection data sets (Mitrovica & Forte, 2004). The values of $\eta_{lm} = 5 \times 10^{22}$ Pa s are consistent with recent estimates from GIA studies based on far-field sea level data by Lambeck et al. (2014) and from LGM sea levels at Barbados and Bonaparte Gulf and the rate of change of degree-two zonal harmonic of Earth's geopotential due to GIA process by Nakada et al. (2016). More recent analyses using GIA data sets due to the last deglaciation yield a deep mantle viscosity of $\sim 10^{23}$ Pa s (Lau et al., 2016; Nakada & Okuno, 2016; Nakada et al., 2018). We therefore adopt a two-layer lower mantle viscosity model defined by $\eta_{670,1191} = 5 \times 10^{21}$ Pa s (viscosity for 670–1191 km depth) and $\eta_{1191,2891} = 5 \times 10^{22}$ Pa s (viscosity for 1191–2891 km depth). The values for $H$and η_{um} are the same as those for the simple three-layer viscosity model. Creveling and Mitrovica (2014) adopted lower mantle viscosities of 5×10^{21} and 2×10^{22} Pa s and evaluated the RSL change relative to a reference time of up to 100 kyr after the complete melt. The highest lower mantle viscosity adopted here is 5×10^{22} Pa s, and we therefore evaluate the RSL change relative to sea level predicted at a reference time of 1 Myr after the complete melt. We ran tests by calculating RSL over longer periods than 1 Myr, and did not see significant changes in the predicted RSL changes. From the above, we see that these parameters for our earth models are deduced for the last Ice Age. Since the earth has been cooling and mantle viscosity is temperature-dependent, the parameters for lithospheric thickness and mantle viscosities should be changing with time too. In Section 3.4.1, we will investigate the effects of this change in average temperature between the Marinoan and the present.

We explain geography/topography models adopted here. The continental distribution, topography of the land, and ocean bathymetry are uncertain yet important in evaluating the RSL changes at 635 Ma. Here we adopt the continental distribution of the 635 Ma from Li et al. (2013) (see Figure 3.3a) and the ratio of ocean area over Earth's surface area is 0.73. The assumed topography at the reference time (initial topography prior to Marinoan snowball glaciation) is based on mean values in modern topography and is shown in Figure 3.4a. This topography model is the same as that used by Creveling and Mitrovica (2014). The continental margin areas shallower than $\sim$ –1000 m depth (Figure 3.4a) are main depositional places of cap dolostones for sedimentary-inferred RSL changes. Particularly, the post-deglacial RSL changes examined in this study areinferred from cap dolostones for the continental shelf areas. We therefore examine the impacts of the coastline geometry and ocean bathymetry and their uncertainties on RSL changes by considering cases with a gulf or a peninsula. A paleotopography TP(x, t) at a time t and position x, which is required in discussing sedimentary-inferred RSL change, is related to the RSL(x, t) by TP(x, t) = T(x) + I(x, t) – RSL(x, t) where T(x) and I(x, t) are the topography at the reference time and the grounded ice thickness, respectively (e.g. Lambeck, 1997). Our studied GIA-based RSL changes occurred in a total period of less than 1 Myr, from the syn- to post-deglacial phases. The mean topography will change with time, but we think that those long-term changes probably introduce uncertainties less than what the different coastline geometry models would in our modeling study.

Next, we explain the ice model (see Figures 3.1b–3.1c). We assume that ice covers all continents during glacial maximum and the total ESL change is 1000 m, as assumed by Creveling and Mitrovica (2014). From the conservation of ice and water mass for the assumed ocean area (73% of the Earth's surface area), we get a mean ice thickness of about 3000 m. ESL linearly decreases within a period of 1 Myr followed by a constant value of –1000 m for a period of 10 Myr reflecting a full snowball phase (Figure 3.1b). In the syn-deglacial phase, we assume a globally synchronous melting for all ice sheets, which is one of the cases considered by Creveling and Mitrovica (2014), and ESL linearly increases starting at

the onset of syn-deglacial phase. The duration of syn-deglaciation is represented by T_d. The value of T_d is treated as variable. Rapid deglaciation with a duration of 2–10 kyr has been inferred from ice sheet dynamics (Hyde et al., 2000) and by analogy with Quaternary deglaciation (Hoffman et al., 2007). Such a rapid deglaciation is also consistent with an estimate of $T_d \sim 6$ kyr based on a paleohydraulic analysis of wave ripples and tidal laminae of the Elatina Formation, Australia (Myrow et al., 2018). Paleomagnetic polarity reversals from the analyses of cap dolostones suggest a deposition duration of longer than 100 kyr (Trindade et al., 2003; Kilner et al., 2005; Hoffman et al., 2007), although this inference is not necessarily equal to the syn-deglacial duration. On the other hand, Creveling et al. (2016) suggested that the cap carbonate platform of the Noonday Formation in SE California records crustal rebound (1–100 kyr) for the whole syn-deglacial phase. Here, we adopt T_d = 2, 5, 7.5, 10, 20, 50, and 100 kyr to examine its effects on RSL change. The distribution of ice thickness is constructed based on the method by Lambeck (1993) in which the maximum ice thickness at the center of ice sheet is proportional to the square-root of the distance of the ice margin from the center (Paterson, 1969). The grounded ice thickness distribution at the maximum glaciation is shown in Figure 3.1c. The grounded ice at this phase covers all continents and continental shelves and also continental slope areas shallower than $\sim$ –1000 m depth (Figure 3.1a) as inferred from ESL value shown in Figure 3.1b. That is, these continental margin areas would be main depositional places for cap dolostones in the syn- and/or post-deglacial phases. The impacts of their uncertainties on RSL changes are examined based on a coastline geometry model with a gulf or a peninsula. Here the glaciated area at an arbitrary time is estimated based on an assumption that the glaciated area decreases in proportion to the ice volume derived from the ESL component (Nakada et al., 2016).

Finally, our model carries an assumption in calculating Earth's rotation and rotational feedback on sea level change. Changes in Earth's rotational axis due to GIA-based Earth deformation perturb the centrifugal potential causing the redistribution of water load, which also causes an additional solid Earth deformation (Milne & Mitrovica, 1996; Mitrovica et al., 2005). The 635 Ma paleogeographic reconstruction adopted here (Li et al., 2013) assumes

that the geomagnetic pole approximates the position of the geographic pole. Here we assume that the position of the rotation axis at the onset of the snowball glaciation was coincident with the geographic pole for the 635 Ma paleogeographic reconstruction (Figure 3.1c).

3.3 Results

In this section, we report the syn- and post-deglacial RSL changes by considering the impacts of coastline geometry, syn-deglacial duration and mantle viscosity on the syn- and post-deglacial RSL drops. It would be useful to mention sea level components for GIA-based RSL change before discussing the results. The RSL change is contributed by eustatic sea level (ice-volume equivalent sea level) component (RSL_{esl}, see Figure 3.1b), sea level component due to the gravitational attraction between ice sheet and seawater loads (RSL_{att}), and the viscoelastic response of the Earth to ice sheet (RSL_{ice}) and seawater (RSL_{water}) loads, i.e., $RSL = RSL_{esl} + RSL_{att} + RSL_{ice} + RSL_{water}$ (e.g. Farrell and Clark, 1976; Nakada and Lambeck, 1987). In this study, the term RSL_{water} includes the contribution to sea level change from Earth's rotation. The terms RSL_{esl} and RSL_{att} are zero in the post-deglacial phase, and the RSL_{att} term was proposed by Hoffman and Macdonald (2010) to explain the regression interrupting the transgressive cap dolostone sequence in Namibia.

Also, we briefly explain the relaxation process of the Earth to the loading. The relaxation process is approximately described as follows (e.g. Wu & Peltier, 1982): the relaxation proceeds through the Earth's deformation associated with the surface displacement (M0 mode) followed by the Earth's deformation associated with the return of the core-mantle boundary (CMB) to its undeformed horizontal state (C0 mode). If the density discontinuity at 670 km depth behaves as a chemical boundary as assumed here, and also assumed in most GIA studies (e.g. Lambeck et al., 2014), the relaxation should proceed through the Earth's deformation in associated with the return of the 670 km density discontinuity to its undeformed position (M1 mode). The impact of the M1 mode is, however, negligible if the 670 km density discontinuity is not a chemical boundary but a phase boundary (e.g. Johnston et al., 1997). L0 mode is related to the presence of the elastic lithosphere. These processes depend

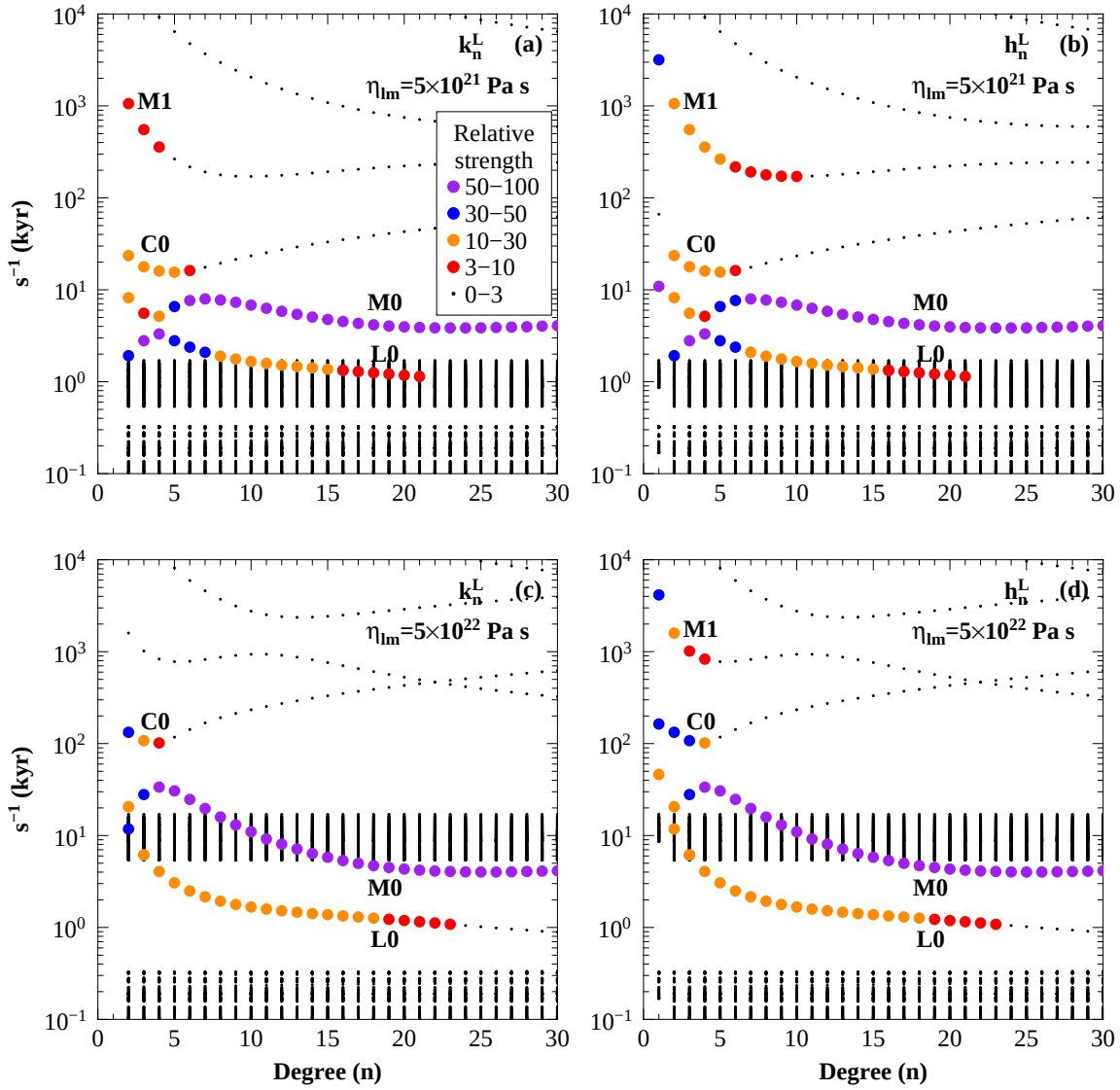

Figure 3.2. The relaxation time for load Love numbers k_2^L and h_2^L based on the model with H = 65 km, $\eta_{um} = 4 \times 10^{20}$ and $\eta_{lm} = (5, 50) \times 10^{21}$ Pa s.

on the viscosity structure of the mantle and the magnitude of density jumps at the boundaries. Figure 3.2 shows the relaxation time for load Love numbers k_2^L and h_2^L. The M0 mode is dominant over degree n, and the relaxation time increases with increasing the wavelength. For long-wavelength (low-degree), the deep part relaxation processes are significant.

This section is organized as follows. In Section 3.3.1, we show the syn-deglacial RSL drop

by considering the impact of coastline geometry on the syn-deglacial RSL change. In Section 3.3.2, we demonstrate the post-deglacial RSL change by focusing on cases with an RSL drop followed by a transgression in the post-deglacial phase, a pattern inferred from sedimentary records such as those in South China. In Section 3.3.2.1, we show that RSL change in South China is affected significantly by Earth's rotation and that RSL changes at low-latitude regions are driven largely by the collapse of the peripheral bulge. In Section 3.3.2.2, we examine the sensitivities of RSL change in South China to mantle viscosity, syn-deglacial duration and changes in the location of South China. In Section 3.3.2.3, we examine the sensitivities of RSL changes at low-latitude regions to coastline geometry, mantle viscosity and syn-deglacial duration.

3.3.1 Syn-deglacial RSL change

In the syn-deglacial phase, the continental slope would be a main depositional place for cap dolostones. Here we examine the GIA-based syn-deglacial RSL change for the continental slope by considering an episode of regression interrupting a cap dolostone transgressive sequence inferred from the stratigraphic studies of cap dolostones in Namibia. Creveling and Mitrovica (2014) analyzed the syn-deglacial RSL drop in detail, and they indicated that the RSL drop interrupting a cap dolostone transgressive sequence is only one of the GIA-based RSL patterns and it can be attributed to one of the three processes (or their combination) of local melting, crustal uplift in regions of significant ice loss, and an extended syn-deglacial phase of duration ~50 kyr or greater, with all scenarios of RSL drop to be confined to the syn-deglacial phase. Adopting a viscosity model with H = 65 km, $\eta_{um} = 4 \times 10^{20}$ Pa s, $\eta_{lm} = 10^{22}$ Pa s and a syn-deglacial duration of 20 kyr (T_d = 20 kyr), our model predicts an RSL drop followed by transgression in the syn-deglacial phase for shaded blue and gray regions (Figure 3.3). The shaded blue regions (Figures 3.3d–3.3e) signify ocean areas as defined by the paleotopography (i.e., site below sea level at a time when RSL drop occurs), and gray regions signify land areas (i.e., site above sea level at a time when RSL drop occurs). In the following we use "ocean" to refer to points with negative paleotopography values and "land

" to refer to points with positive paleotopography values. Figures 3.3b–3.3e show contour maps of the syn-deglacial RSL drop (red colour) for regions A and C–E in Figure 3.3a. The contour line for the initial topography is shown by the black line. The RSL drops for regions A and C occur within land areas, and those in ocean areas are predicted to occur at the inner part of the gulf in region D and at the channel in region E.

We explore the syn-deglacial RSL changes at sites C1 to C3 in Figure 3.4a. Sites C1 and C2 are located on the coastline and outer edge of the continental shelf at the initial topography, respectively. Site C3, which is located on the continental slope, corresponds to the site in Namibia where Hoffman and Macdonald (2010) inferred an episode of regression interrupting a cap dolostone transgressive sequence. Figure 3.4b shows RSL changes at sites C1 to C3. The RSL changes predicted for ocean sites are shown by solid lines, and those for land sites are shown by dotted lines. The RSL at site C3 in the ocean gradually rises from –20 to 0 kyr, and that for site C1 on land shows an RSL drop with a magnitude of ~30 m from –20 to –17 kyr followed by an RSL rise from –17 to 0 kyr.

We now explore the impact of coastline geometry on the predicted syn-deglacial RSL drop. Within Region C we observe a fall in RSL for land-based sites (Figures 3.4a–3.4b), but the inner part of the gulf in region D clearly shows an RSL drop within the ocean (Figure 3.3d). This is consistent with the results by Creveling and Mitrovica (2014) that regions of significant ice loss are subject to large land rebound and are characterized by the syn-deglacial RSL drop. We also consider the coastline geometry models M1 with a gulf of width and length (4°, 4°) for region C (Figure 3.4c), and M2 (Figure 3.4e) characterized by a peninsula of width and length (4°, 4°). The peninsula in M2 is located on the continental shelf (see 0 m contour line for the topography in Figure 3.4e). These coastline geometry models reflect uncertainties of the paleogeography and have analogies in present-day coastline geometries. For example, the gulf for M1 is like Bay of Biscay and the peninsular for M2 is like Grand Banks of Newfoundland.

Our coastline geometry model M1 predicts a syn-deglacial RSL drop within the continental slope (Figure 3.4c). This is because the crustal uplift (RSL fall) at the continental

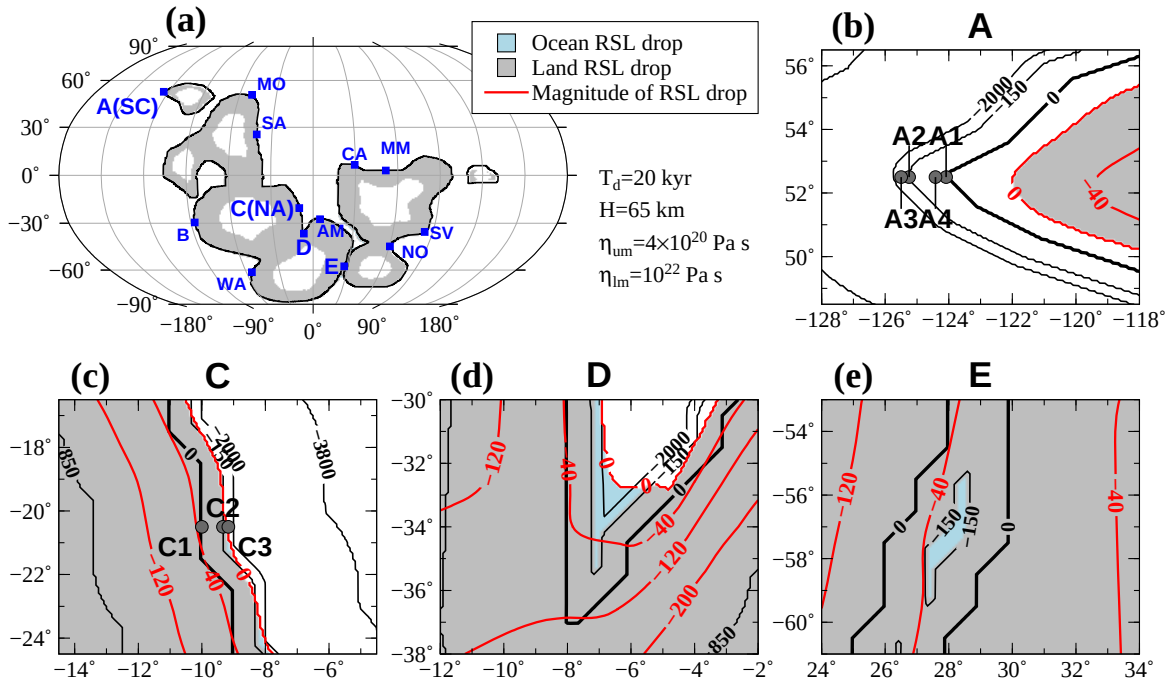

Figure 3.3. (a) Spatial distribution for RSL drop in the syn-deglacial phase based on the model with the coastline geometry model M0, T_d = 20 kyr, H = 65 km, η_{um} = 4 × 10^{20} and η_{lm} = 10^{22} Pa s. Regions lying below sea level that experience a fall in RSL are shaded blue (see panels d and e), and regions lying above sea level that experience a fall in RSL are gray. Labels refer to the following locations: SC - South China; WA - West Africa; MO - Zavkhan Terrane of southwestern Mongolia; SA - South Australia; NA - Namibia; AM - southern Amazon; CA - California; MM - Mackenzie Mountains, northwestern Canada; SV - Svalbard; NO - East Finnmark of Norway. (b) – (e) The contour maps of the RSL drop (red colour) in the syn-deglacial phase for regions A and C–E. The contour line for the initial topography is shown by the black line.

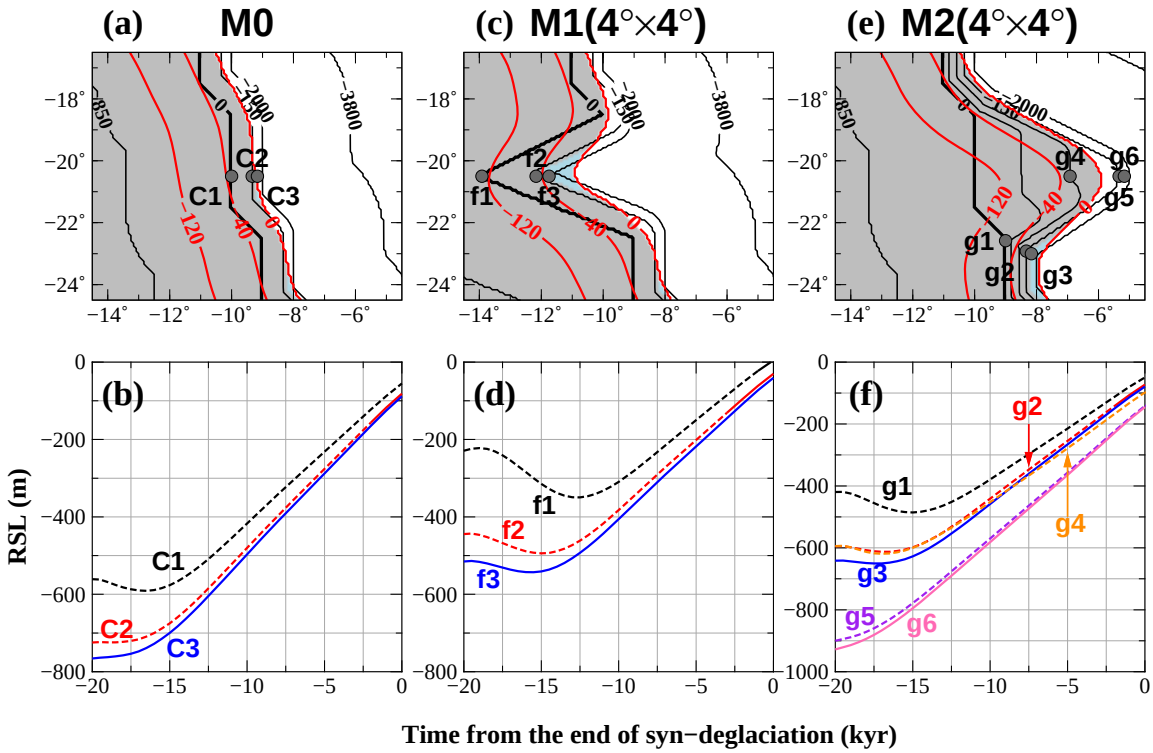

Figure 3.4. (a) Contour map of the RSL drop (red colour) in the syn-deglacial phase for regions C based on the coastline geometry model M0. Regions lying below sea level that experience a fall in RSL are shaded blue (see panels c and e), and regions lying above sea level that experience a fall in RSL are gray. The contour line for the initial topography is shown by the black line. (b) RSL changes at sites C1–C3 shown in panel (a) based on the model with T_d = 20 kyr, H = 65 km, $\eta_{um} = 4 \times 10^{20}$ and $\eta_{lm} = 10^{22}$ Pa s. The RSL change predicted at ocean site for the paleotopography is shown by the solid line, and that at land site is shown by the dotted line. (c) – (d) As in panels (a) – (b), except for M1. (e) – (f) As in panels (a) – (b), except for M2. Sites C1(f1, g1), C2(f2, g2, g5) and C3(f3, g3, g6) are located on the coastline, outer edge of the continental shelf and continental slope at the initial topography, respectively.

slope site for M1 is significantly larger than that for M0, and consequently, the magnitude of RSL fall due to the loss of gravitational attraction between ice and ocean loads (RSL_{att} term) and local crustal uplift (RSL_{ice} term) exceeds the eustatic sea level rise (RSL_{esl} term). The predicted syn-deglacial RSL drop is consistent with a regression in the syn-deglacial phase inferred from the cap dolostones on the lower-slope sections of the Congo and Kalahari cratons (Hoffman & Macdonald, 2010). We next consider the coastline geometry model M2 (Figures 3.4e–3.4f). An RSL drop within the ocean is not predicted for the region around the tip of the peninsula (site g6), but it is predicted for the region around the base of the peninsula with a coastline geometry similar to a gulf (site g3). Although we do not show the results, the magnitude of the RSL drop increases as the size of the gulf and ratio of the length to width of the gulf is increased. However, our numerical experiments for such coastline geometry models do not predict a syn-deglacial RSL drop within the continental shelf because the continental shelf lies above sea level until the late stage of the syn-deglacial phase. This remains true if the syn-deglacial RSL drop is attributed to a rapid localized melting event, as indicated by Creveling and Mitrovica (2014).

3.3.2 Post-deglacial RSL change

3.3.2.1 Impacts of Earth's rotation and collapse of peripheral bulge on RSL change

In the post-deglacial phase, continental shelf becomes a main depositional setting for cap dolostones. Here we examine the post-deglacial RSL change in continental shelf areas by focusing on cases with an RSL drop followed by a transgression in the post-deglacial phase, a pattern inferred from sedimentary records such as those in South China (Zhou et al., 2010). Figures 3.5a–3.5c show the spatial and temporal variations of post-deglacial RSL changes (black contour lines) based on a model with T_d = 2 kyr, H = 65 km, $\eta_{um} = 4 \times 10^{20}$ Pa s, $\eta_{lm} = 5 \times 10^{22}$ Pa s and coastline geometry model M0. We explain these spatial variations by considering GIA response to surface load distribution (Figure 3.6). Ice and water loads are assumed to be zero before the glaciation. In the glacial phase, ice load is positive in the continent and water load is negative in the ocean. Both the ice loading and the water un-

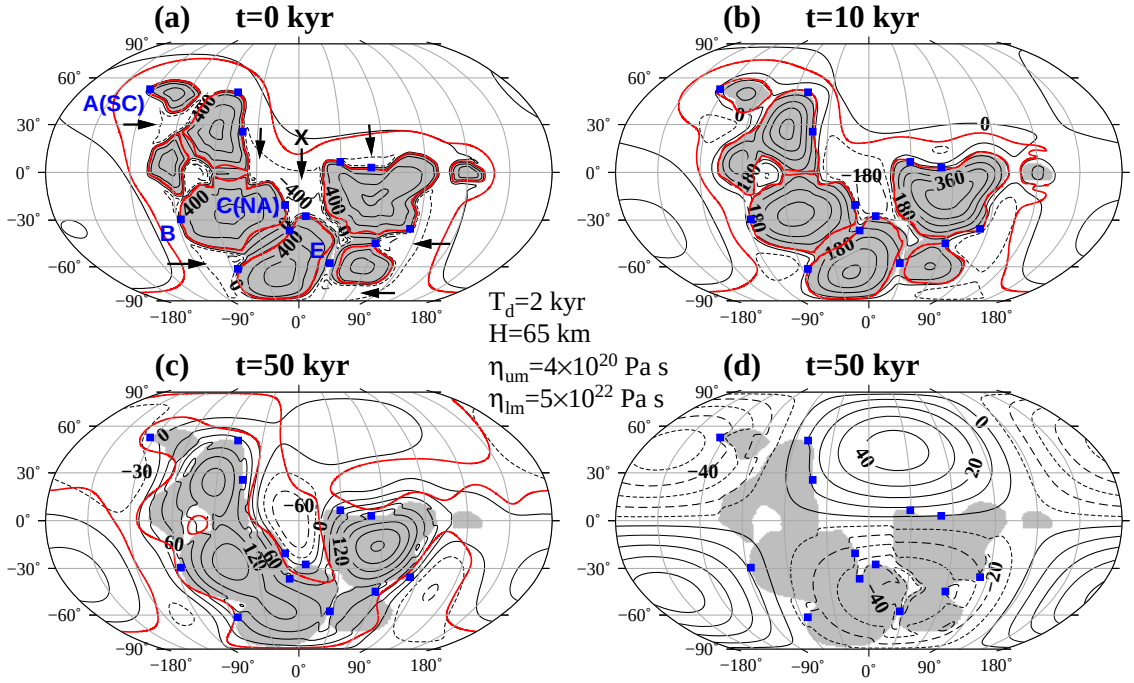

Figure 3.5. (a) – (c) RSL changes at t = 0, 10 and 50 kyr and (d) rotational component at t = 50 kyr based on the model with the coastline geometry model M0, T_d = 2 kyr, H = 65 km, η_{um} = 4 ×10^{20} and η_{lm} = 5 ×10^{22} Pa s. Contour intervals for panels (a) – (d), solid black line for positive value and dashed black one for the negative, are 200, 90, 30 and 10 m, respectively. Red line shows the boundary between the RSL fall region and RSL rise one (referred to as hinge-line here). Labels for panel (a) are the same as those for Figure 1a. The gray regions represent land areas for the initial topography.

loading cause downward crustal movement in the continent and upward crustal movement in the ocean. Here we use "peripheral bulge" to refer to the upward displacement in the ocean due to both loads. In the post-deglacial RSL changes shown in Figures 3.5a–3.5c, continental regions exhibit RSL fall due to the crustal rebound, and their peripheral areas exhibit RSL rise due mainly to the crustal subsidence (collapse of the peripheral bulge). Red lines show the boundary between the RSL fall region and the RSL rise one (referred to as hinge-line here). Continental margins are almost equivalent with the hinge-lines at t = 0

kyr. Over time, the hinge-lines move outward or seaward as a whole and long-wavelength RSL components become dominant (for example, see RSL changes at t = 50 kyr in Figure 3.5c). These temporal and spatial variations are related to the time-dependent behavior of the peripheral bulge when the adopted viscosity model is characterized by $\eta_{lm} \gg \eta_{um}$ (e.g. Cathles, 1975), and may be crucial in interpreting the post-deglacial RSL change for some continental shelf areas, a depositional location for cap dolostones. Creveling and Mitrovica (2014) discussed the post-deglacial RSL change, but did not describe sedimentary-inferred non-monotonic post-deglacial RSL behavior such as that inferred in South China. Here we explore the non-monotonic RSL behavior by considering the impact of the collapse of peripheral bulge, Earth's rotation, coastline geometry and the paleogeography on the GIA-based RSL change.

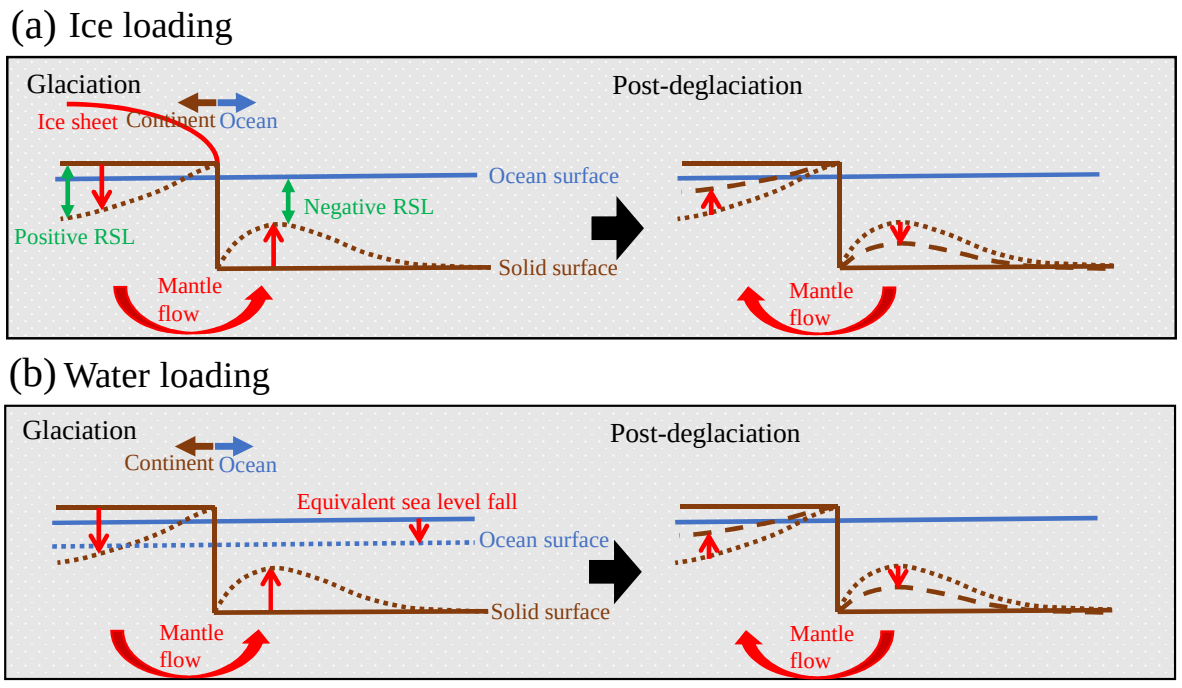

Figure 3.6. Schematic illustrations of GIA response to ice and water loads.

Evaluating a GIA-based RSL change needs to take Earth's rotation into consideration (Milne & Mitrovica, 1996). Figure 3.5d shows the difference between the RSL changes at t = 50 kyr for rotating and non-rotating Earth models. The impact of Earth's rotation on

the RSL change is dominated by a degree-two and order-one harmonic signal. The RSL at t = 50 kyr for region A is ~ –30 m (Figure 3.5c) and its rotational component is ~ –40 m (Figure 3.5d), implying that the magnitude of the rotational component is significantly larger than the other components associated with ice sheet and seawater loads (~10 m). At region E, located close to the opposite side of region A, the RSL change at t = 50 kyr is positive and its rotational component is negative, implying that its RSL change is dominated by ice unloading and meltwater loading effects. That is, the Earth's rotation has significant impacts on the RSL change at mid-latitude and isolated region, like South China.

The peak value for an adopted ESL history model (Figure 3.1b) depends insignificantly on the ice thickness distribution, geography and topography models, but is proportional to the peak ESL amplitude and is affected by the presence of a saw-tooth ESL history. Figure 3.7 shows rotational component at t = 50 kyr based on the viscosity model with H = 65 km, η_{um} = 4 ×10^{20} and η_{lm} = 5 ×10^{22} Pa s. We examine the rotational effects on the RSL change based on six geography/topography and ice sheet models (models A–F). Model A is the same as that used in Figure 3.5d, except for T_d = 10 kyr. The peak value of rotational component for model A (Figure 3.7a) is ~±50 m and almost the same as that shown in Figure 3.5d. The total ESL change for model B is 130 m and the ESL value at time t is (130/1000) × ESL value at time t for the model shown in Figure 3.1b. The glaciated areas at time t are the same as those for model A, and the ice thickness distribution is based on the ESL history. The total ESL change of 130 m corresponds to that for the last deglaciation inferred from the GIA studies by ANU group (e.g., Lambeck et al., 2014), that is, ~1/8 (130/1000) of that for the Marinoan snowball Earth. The peak value for model B (Figure 3.7b) is ~±6 m, that is, ~1/8 of that for model A (Figure 3.7a). That is, the peak value is proportion to the total ESL change.

Model C is defined by the ESL history with a 100 kyr glaciation phase (growth phase of the ice sheet), 1 Myr full glacial phase and 10 kyr deglacial phase shown by the black solid line in Figure 3.7c. The glaciated areas and the ice thickness distribution at time t are based on the ESL value at time t as discussed in the text. The peak value for model C (Figure 3.7d) is ~±6 m and almost the same as that for model B (Figure 3.7b). This is a natural consequence

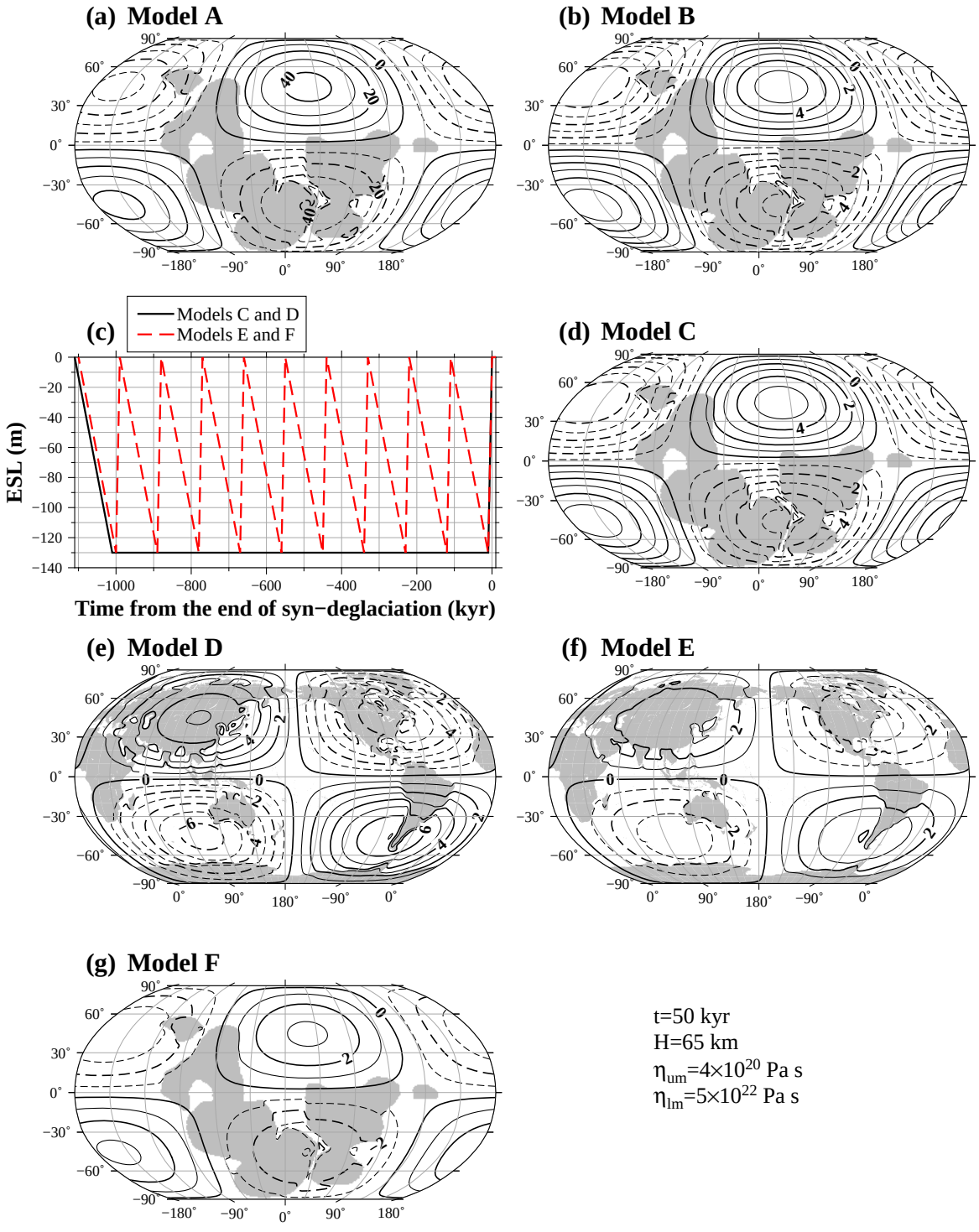

Figure 3.7. Rotational component at t = 50 kyr based on the viscosity model with H = 65 km, η_{um} = 4 ×10^{20} and η_{lm} = 5 ×10^{22} Pa s.

of an adopted reference time of 1 Myr. Model D uses the present geography and topography models and the ice thickness distribution at the LGM for the ice model IA20 (Figure 1.2a) nearly identical to the ANU model by Lambeck et al. (2014) Nakada et al., 2018). The ESL history for model D is the same as that for model C (black solid line in Figure 3.7c), and the glaciated areas and the ice thickness distribution at time t are based on the ESL value at time t as discussed in the text. The peak value for model D (Figure 3.7e) is $\sim\pm6$ m and almost the same as that for model C (Figure 3.7d). That is, the peak value depends insignificantly on the ice thickness distribution model and geography/topography models related to the water load.

The ESL history for models E and F is defined by a simple 10 saw-tooth glacial cycle model with a 100 kyr glaciation phase and a 10 kyr deglaciation phase characterizing the Quaternary glaciation (red dashed line in Figure 3.7c). The glaciated areas and the ice thickness distribution at time t are also based on the ESL value at time t as discussed in the text. The peak value for model E (Figure 3.7f) is $\sim\pm3$ m, $\sim1/2$ of that for model D (Figure 3.7e). That is, the peak value is significantly affected by the ESL history, which is true for the results using models C and F.

Next, we examine the spatial distribution of non-monotonic RSL behavior by considering the time-dependent hinge-line movement. Figures 3.8a–3.8d show the transition time from post-deglacial RSL fall to rise for four lower mantle viscosity models. We only show the transition that occurs on land or continental shelf for $t \leq 80$ kyr. The transition area increases with increasing lower mantle viscosity, and the general pattern for $\eta_{lm} = 5 \times 10^{22}$ Pa s is similar to that for a two-layer lower mantle viscosity model with $\eta_{670,1191} = 5 \times 10^{21}$ and $\eta_{1191,2891} = 5 \times 10^{22}$ Pa s. Figures 3.8e–3.8g show the hinge-lines at $t = 0$, 10, 20, 50 and 70 kyr for regions L–N (Figure 3.8c) based on the model with $\eta_{lm} = 5 \times 10^{22}$ Pa s. We first examine the overall relationship between RSL change and hinge-line movement by considering typical spatial patterns of hinge-line movement predicted for regions M and N. Figure 3.9a illustrates the relationship between RSL change and outward migration of hinge-point for a period from 0 to 30 kyr based on the RSL change for the transect shown in Figure 3.8f. The hinge-points at $t = 0$ and 30 kyr (X0 and X30) divide the RSL change into three

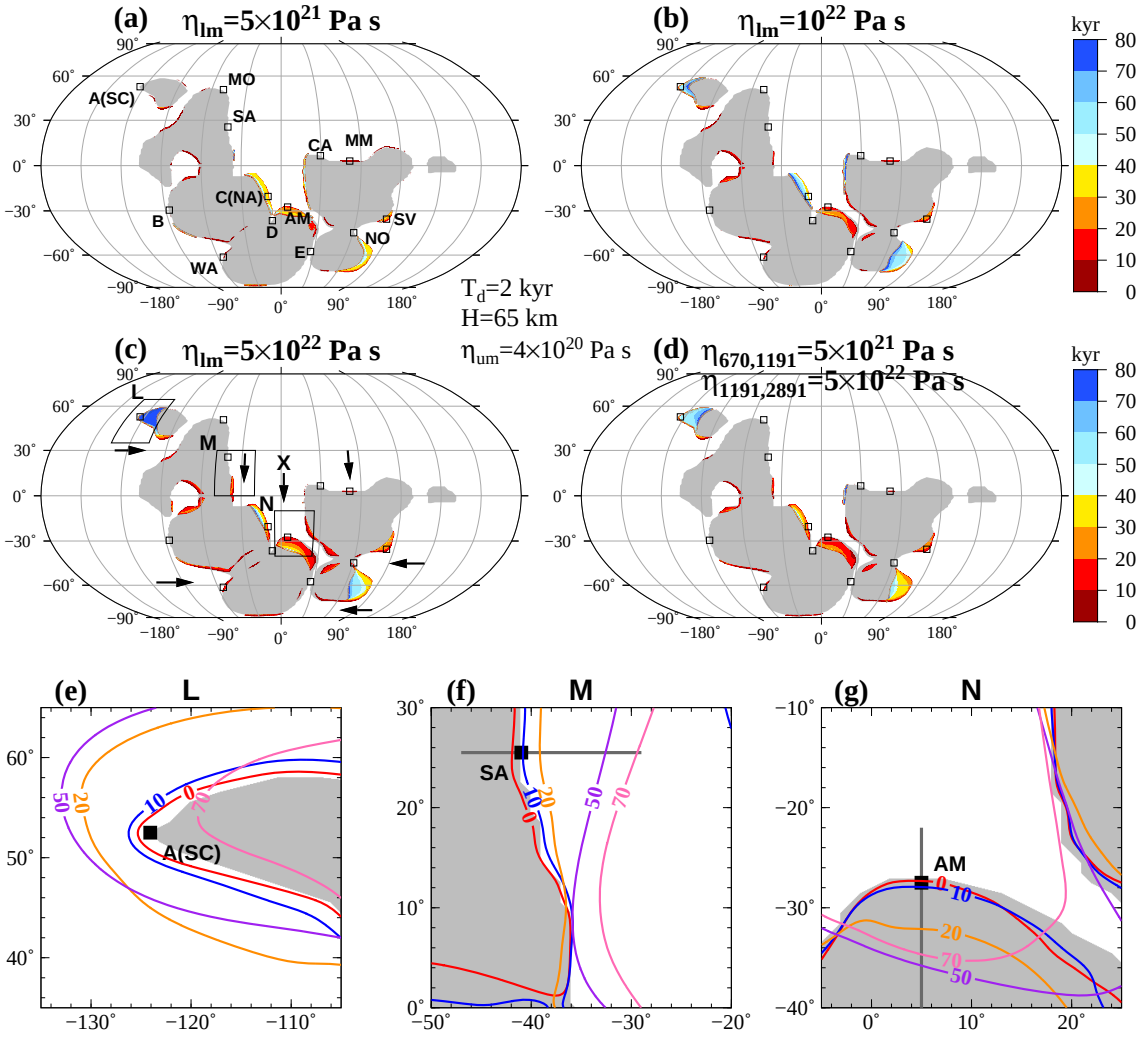

Figure 3.8. (a) – (d) The transition time from post-deglacial RSL fall to rise based on the coastline geometry model M0, T_d = 2 kyr, H = 65 km and η_{um} = 4 ×10^{20} Pa s. (a) – (c) The transition time for simple three-layer viscosity models with η_{lm} = (5, 10, 50) × 10^{21} Pa s and (d) the transition time for a two-layer lower mantle viscosity model with $\eta_{670,1191}$ = 5 × 10^{21} and $\eta_{1191,2891}$ = 5 × 10^{22} Pa s. Labels for panel (a) are the same as those for Figure 1a. (e) – (g) The hinge-lines at t = 0, 10, 20, 50 and 70 kyr for regions L–N in panel (c) based on the model with η_{lm} = 5 × 10^{22} Pa s. The gray regions represent land areas for the initial topography.

types; RSL changes in regions I, IIa and III. RSL change in region I, landward side for the hinge-points from 0 to 30 kyr, is characterized by an RSL fall from 0 to 30 kyr. RSL change in region IIa, seaward side for X0 and landward side for X30, is characterized by an RSL rise followed by an RSL fall. RSL change in region III, seaward side for the hinge-points at t = 0 and 30 kyr, is characterized by an RSL rise from 0 to 30 kyr. Figure 3.9b illustrates the RSL change for the transect shown in Figure 3.8g. RSL patterns in regions I and III are the same as those for the outward migration of hinge-point. However, RSL change in region IIb, landward side for X0 and seaward side for X30, is characterized by an RSL drop followed by an RSL rise.

We next consider the post-deglacial RSL change in regions L, M and N (Figures 3.8e–3.8g). The hinge-line for region L (South China), which is affected significantly by Earth's rotation (Figure 3.5d), migrates outward for $t \leq 50$ kyr and migrates inward for $t > 50$ kyr. Therefore, the RSL change at site A, landward site of the hinge-line for $t \leq 50$ kyr and seaward site for $t > 50$ kyr, shows an RSL fall for $t \leq 50$ kyr and RSL rise for $t > 50$ kyr. We discuss the post-deglacial RSL change in South China in more detail below (Section 3.3.2.2). However, the post-deglacial RSL changes in regions M and N have a negligible RSL contribution from Earth's rotation compared with South China (Figure 3.5d) and the post-deglacial RSL changes are significantly affected by time-dependent behavior of peripheral bulge. The hinge-lines for the northern part of region M show a continuous (monotonic) outward migration with the collapse of peripheral bulge, indicating a monotonic post-deglacial RSL fall on the landward side of the hinge-line at t = 0 kyr and an RSL rise followed by an RSL fall on the seaward side (see Figure 3.9a). The hinge-lines over the southern portion show an inward migration until ~20 kyr and then migrate outward, indicating a non-monotonic RSL behavior characterized by an RSL drop for $t < 20$ kyr and a transgression for $t > 20$ kyr. The hinge-lines for region N show inward migration over a duration longer than 20 kyr (see Figure 3.9b). We can explore the mechanism for the non-monotonic hinge-line movement by considering the impact of the adopted paleogeography model on the RSL change. Region N faces a relatively small ocean surrounded by continents ("X" in Figures 3.5a and 3.8c referred to as ocean "X"

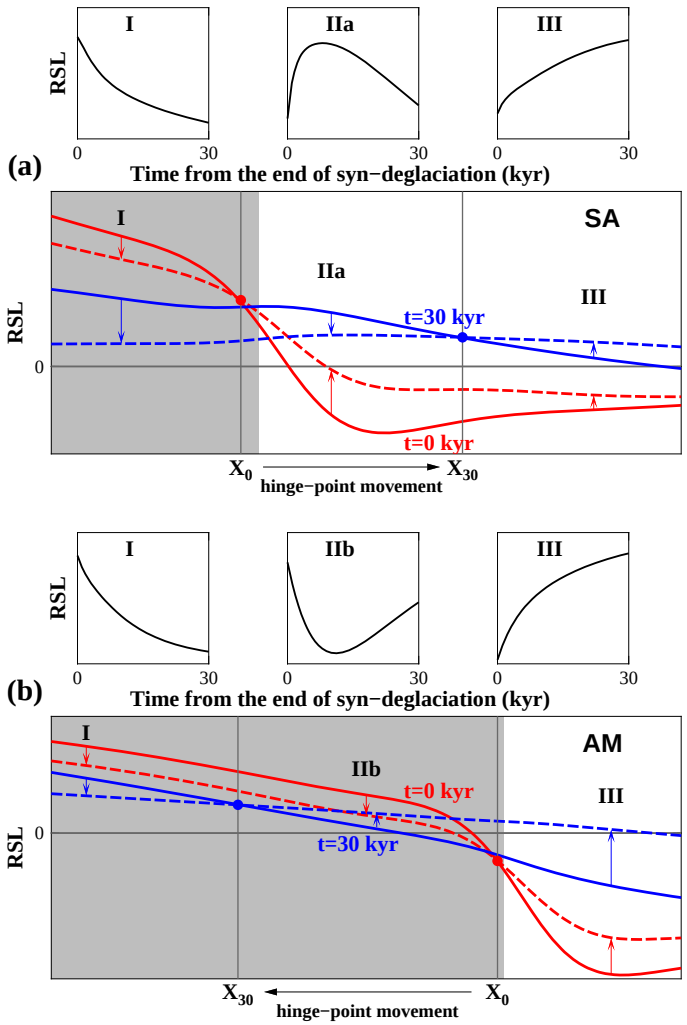

Figure 3.9. (a) – (b) Schematic illustrations of the relationship between RSL change and hinge-point movement based on the RSL change for the transect (dark gray line) shown in Figures 3.8f and 3.8g. RSL changes at t = 0 and 30 kyr are shown by red and blue solid lines, respectively, and RSL changes at t = 1 and 35 kyr are shown by red and blue dashed lines, respectively. Note that the difference between solid and dotted lines are enlarged in order to emphasize the hinge points. The hinge-points at t = 0 and 30 kyr (X0 and X30) divide the RSL change into three types; RSL changes in regions I, IIa and III for panel (a) and RSL changes in regions I, IIb and III for panel (b). The gray regions represent land areas for the initial topography.

here). The inward migration of the hinge-line is primarily related to the subsidence of the ocean "X" due to ice unloading and meltwater loading effects as inferred from RSL changes predicted for the ocean "X" (Figures 3.5b–3.5c). That is, the GIA response with a spatial-scale of ocean "X" is probably a main cause for the non-monotonic hinge-line movement for regions N. This is true for other regions showing non-monotonic RSL behavior, which face a small ocean surrounded by continents such as the ocean "X" or oceans (gulfs) indicated by arrows in Figure 3.8c (see also RSL changes in Figure 3.5b for these regions). We discuss the post-deglacial RSL changes for these regions in Section 3.3.2.3 in more detail.

3.3.2.2 Post-deglacial RSL change in South China

We discuss the post-deglacial RSL change in South China. The following results are consistent with those derived from the hinge-line movement shown in Figure 3.8. Figure 3.10a shows an enlarged map for region A based on the coastline geometry model M0. Sites A1 and A2 are located on the coastline and outer edge of the continental shelf in the case of the initial topography, respectively. A post-deglacial transgression is not predicted for the viscosity model with $\eta_{lm} = 5 \times 10^{21}$ Pa s (Figure 3.10b), and is not clear for the model with $\eta_{lm} = 10^{22}$ Pa s (Figure 3.10c) (see also Figures 3.8a–3.8b). However, the viscosity model with $\eta_{lm} = 5 \times 10^{22}$ Pa s predicts an RSL drop followed by transgression in the post-deglacial phase over the continental shelf area between sites A1 and A2 (Figure 3.10d). The RSL change at site A4 is nearly identical to that for site A1. Site A4 lies below sea level in the post-deglacial phase (denoted by a solid line), but site A1 lies above sea level from 30 to 200 kyr (denoted by a dotted line). That is, the region between sites A1 and A4 undergoes subaerial exposure at the regression-transgression transition. In this region, cap dolostones may undergo karstic dissolution, which is consistent with observed karst-like dissolution features at the top of the cap dolostones in South China. Zhou et al. (2010) interpreted these as requiring a brief disruption or hiatus in carbonate sedimentation, possibly reflecting a brief time window of an RSL drop.

We next consider a two-layer lower mantle viscosity model with $\eta_{670,1191} = 5 \times 10^{21}$ and

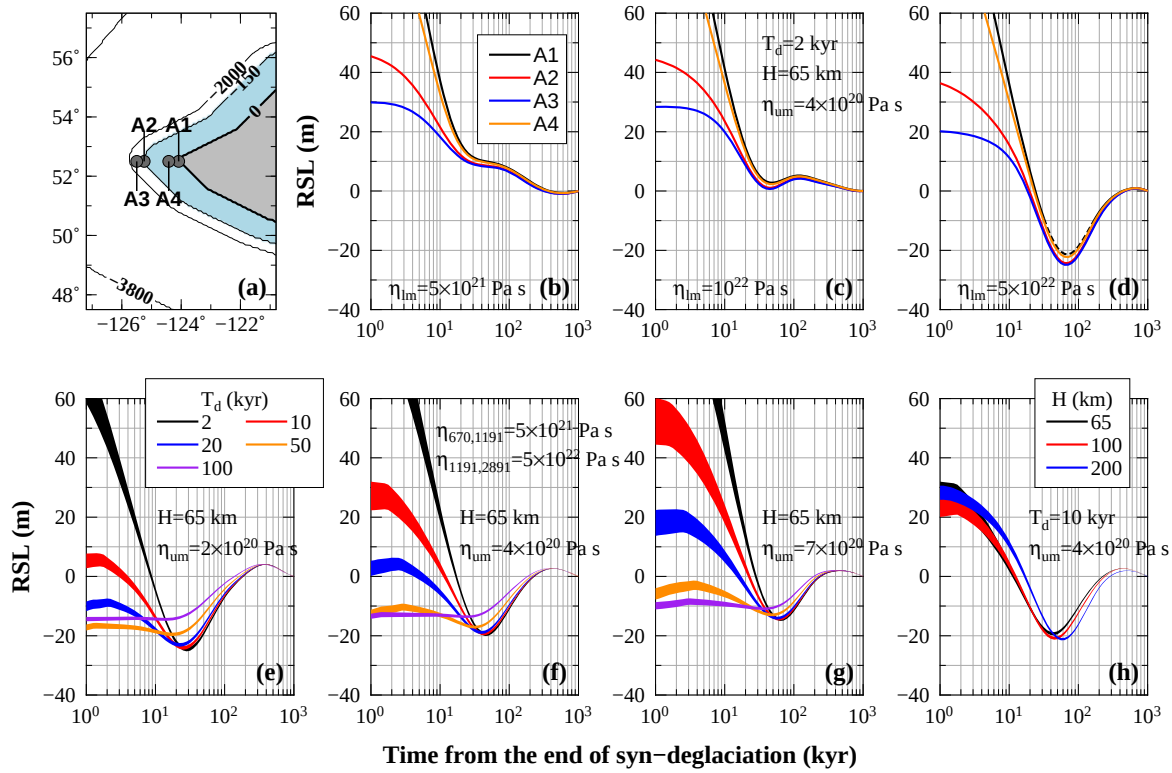

Figure 3.10. (a) An enlarged map for region A. The shaded blue region represents the continental shelf for the initial topography and the gray regions represent land areas. The contour line for the initial topography is shown by the black line. (b) – (d) RSL changes at sites A1–A4 based on the models with T_d = 2 kyr, H = 65 km, $\eta_{um} = 4 \times 10^{20}$ Pa s and η_{lm} = (5, 10, 50) $\times 10^{21}$ Pa s. The RSL change predicted at ocean site for the paleotopography is shown by the solid line, and that at land site is shown by the dotted line. (e) – (h) RSL changes for the region between sites A1 and A4 based on the model with $\eta_{670,1191} = 5 \times 10^{21}$ and $\eta_{1191,2891} = 5 \times 10^{22}$ Pa s. (e) – (g) RSL changes for T_d = (2, 10, 20, 50, 100) kyr, H = 65 km and η_{um} = (2, 4, 7) $\times 10^{20}$ Pa s and (h) RSL changes for T_d = 10 kyr, H = (65, 100, 200) km and η_{um} = 4×10^{20} Pa s. The coastline geometry model is M0.

$\eta_{1191,2891} = 5 \times 10^{22}$ Pa s (Figures 3.10e–3.10h). Figures 3.10e–3.10g show the predicted RSL changes between sites A1 and A4 for each T_d value, and those for each Hvalue are shown in Figure 3.10h. The thickness of the lines in Figures 3.10e–3.10h changes with time because the difference between the RSL changes at sites A1 and A4 decreases with time. The two-layer lower mantle viscosity model with $\eta_{um} = 4 \times 10^{20}$ Pa s predicts an RSL drop followed by transgression (black line in Figure 3.10f), as is also predicted for the model with $\eta_{lm} = 5 \times 10^{22}$ and $\eta_{um} = 4 \times 10^{20}$ Pa s (Figure 3.10d). These results indicate that an RSL drop followed by transgression in the post-deglacial phase is robust when we adopt a viscosity of $\sim 5 \times 10^{22}$ Pa s for the deep mantle. We also consider the effects of the lithospheric thickness (H), upper mantle viscosity (η_{um}) and syn-deglacial duration (T_d) on post-deglacial RSL change. The general feature of the RSL change for H = 100 and 200 km is similar to that for H = 65 km (Figure 3.10h). Furthermore, the post-deglacial RSL changes for this region have the same sensitivities to syn-deglacial duration, and a distinct RSL drop is predicted for the models with $T_d \leq 20$ kyr regardless of the upper mantle viscosity (Figures 3.10e–3.10g).

The exact paleogeography of South China or Yangtze Block at ~635 Ma has uncertainties (e.g. Hoffman & Li, 2009; Li et al., 2013). We therefore examine the sensitivity of the predicted RSL change at site A1 to changes in the location of South China (Figure 3.11a). The ten different locations of South China denoted by "P" to "Y" in Figure 3.11a are obtained by shifting the block in longitude by 30° to 270° relative to the original location of South China (location "P"), respectively. With increasing displacement in the longitude direction, the onset time of the second RSL rise increases and the magnitude of the second transgression decreases (Figure 3.11b). A second transgression is not predicted at locations "T" to "Y". This exercise shows that one must take into account uncertainties of the paleogeography when discussing the observationally inferred post-deglacial RSL change in South China. Conversely, it may be possible to put some constraints on the paleogeography from the observationally inferred RSL change.

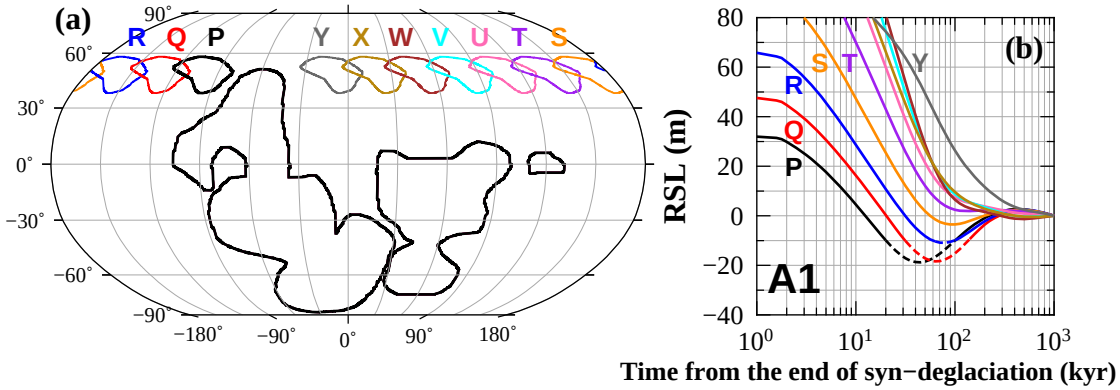

Figure 3.11. Illustrations to show the effects of paleogeography on RSL change in South China based on the model with T_d = 10 kyr, H = 65 km, $\eta_{um} = 4 \times 10^{20}$, $\eta_{670,1191} = 5 \times 10^{21}$ and $\eta_{1191,2891} = 5 \times 10^{22}$ Pa s. (a) Ten different locations of South China denoted by "P" to "Y" obtained by taking the displacement in longitude direction of 30° to 270° relative to the original location of South China (location "P"). (b) The RSL changes at site A1 for locations "P" to "Y" in panel (a). The RSL change predicted at ocean site for the paleotopography is shown by the solid line, and that at land site is shown by the dotted line.

3.3.2.3 Post-deglacial RSL change at low-latitude regions

In this section, we discuss the post-deglacial RSL changes for regions B and C (Figure 3.5a) based on a model with T_d = 2 kyr, H = 65 km, $\eta_{um} = 4 \times 10^{20}$ Pa s, $\eta_{lm} = 5 \times 10^{22}$ Pa s and coastline geometry models M0 and M2 (Figures 3.12 and 3.13). The discussion for region B applies to other monotonic hinge-line movement regions and that for C applies to other non-monotonic ones. The difference between the RSL changes for regions B and C is attributed to the subsidence of the ocean "X" due to the ice-sheet unloading and meltwater loading. We therefore examine the post-deglacial RSL change by decomposing the RSL change into ice ($\mathrm{RSL_{ice}}$) and water ($\mathrm{RSL_{water}}$) loading components, i.e., $\mathrm{RSL} = \mathrm{RSL_{ice}} + \mathrm{RSL_{water}}$. The terms $\mathrm{RSL_{esl}}$ and $\mathrm{RSL_{att}}$ are zero in the post-deglacial phase. The term $\mathrm{RSL_{ice}}$ represents the variation in sea level associated with the loading and unloading of the ice sheets. The term

RSL_{water} represents the contribution to sea level change caused by the seawater unloading and meltwater loading.

Figures 3.12a–3.12g show the hinge-lines at t = 0, 10, 20, 50 and 70 kyr, RSL_{ice} and RSL_{water} terms and RSL change for region B based on the coastline geometry model M0. The RSL changes for this region bear similar RSL patterns as shown in Figure 3.9a. The height of the peripheral bulge relative to the initial topography is approximately given by the negative value of predicted RSL change shown in Figure 3.12d, and the maximum height at t = 0 kyr is ~200 m around –91°E. Those for RSL_{ice} and RSL_{water} terms are ~120 and ~70 m, respectively (Figures 3.12b–3.12c). We next examine the RSL change by considering the RSL_{ice} and RSL_{water} terms shown in Figures 3.12e–3.12g. The RSL changes at ocean sites B4–B7, the maximum height region of the peripheral bulge at t = 0 kyr (Figure 3.12d), show a transgression followed by an RSL drop, which is mainly due to the RSL_{ice} term (e.g. Cathles, 1975). The prediction at coastline site B2 for the initial topography shows a continuous RSL fall in "ocean areas", which is largely due to the RSL_{water} term. The RSL change at site B3 is equally contributed by RSL_{ice} and RSL_{water} terms. These spatial variations are attributed to the outward migration of hinge-line associated with the collapse of the peripheral bulge, resulting in a typical RSL pattern along lines that cross the coastline (Creveling & Mitrovica, 2014).

Paleogeographic reconstructions following Marinoan snowball Earth in Namibia (C in Figure 3.5a) suggest that the lateral distance of the cap dolostone deposition may have extended longer than 100 km over shallow platforms (Hoffman, 2011). We therefore examine the post-deglacial RSL change for the coastline geometry model M2 with a peninsula described by width and length of (4°, 4°) (Figure 3.12h). The RSL changes are affected by local crustal uplift (RSL fall) associated with ice load melting in the peninsula area and crustal movement due to the hinge-line motions (Figure 3.12h). Those at sites b1–b7 are almost the same as those at sites B1–B7 for M0, respectively, as inferred from the hinge-line movement. The migration rate of the hinge-line exhibits significant spatial variability for $t \leq 20$ kyr and the hinge-line at the tip of peninsula is nearly stationary until ~20 kyr. However, the migration

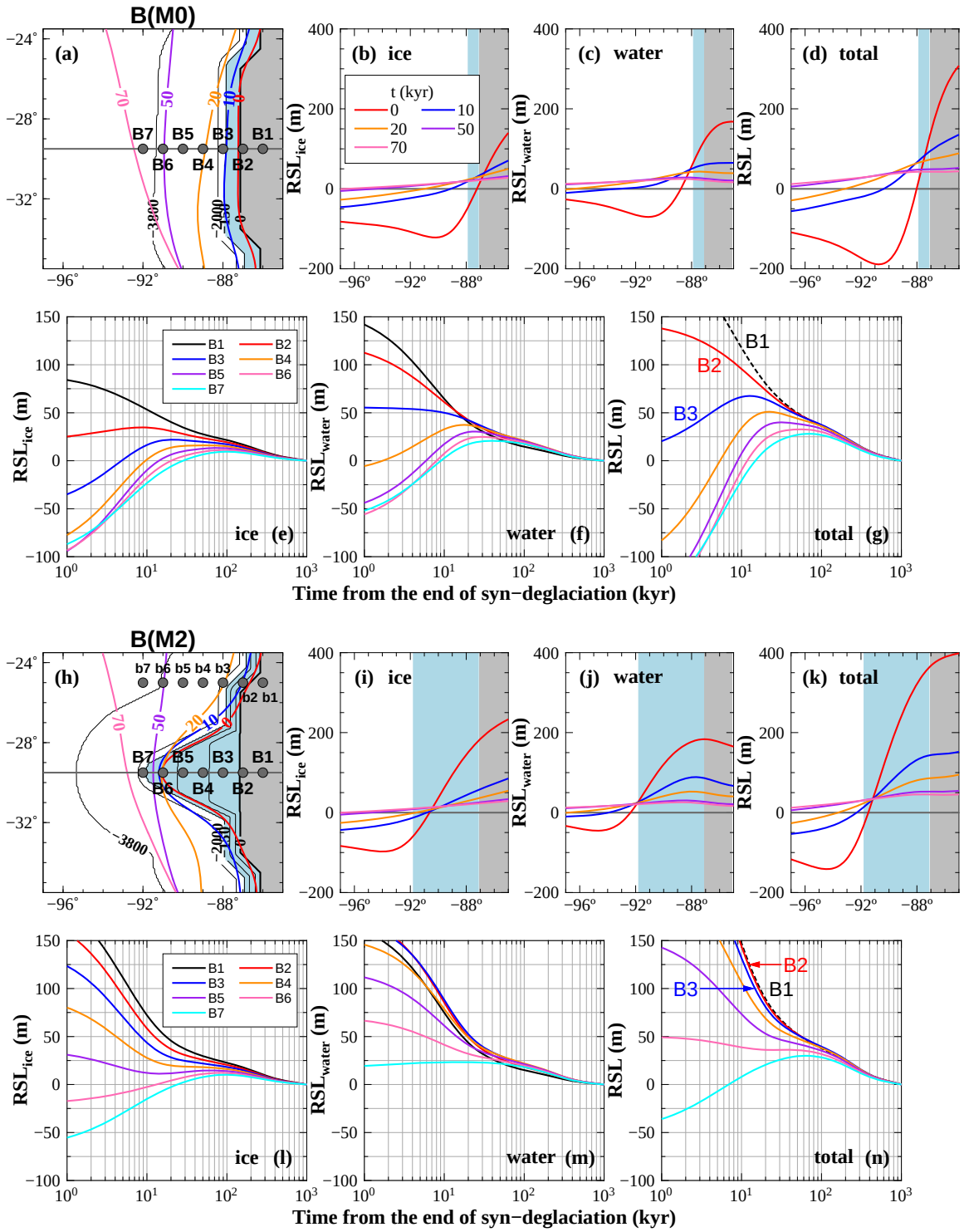
B(M0)
(a)
(b) ice
(c) water
(d) total
t (kyr)
0
10
20
50
70
B7
B5
B3
B1
B6
B4
B2
RSL_ice (m)
RSL_water (m)
RSL (m)
(e) ice
(f) water
(g) total
B(M2)
(h)
(i) ice
(j) water
(k) total
(l) ice
(m) water
(n) total
Time from the end of syn−deglaciation (kyr)

Figure 3.12. (a) Hinge-lines at t = 0, 10, 20, 50 and 70 kyr for region B (see Figure 3.8a). The predictions are based on the model with T_d = 2 kyr, H = 65 km, $\eta_{um} = 4 \times 10^{20}$ Pa s, $\eta_{lm} = 5 \times 10^{22}$ Pa s and coastline geometry model M0. The shaded blue region represents the continental shelf for the initial topography and the gray region represents land area. The contour line for the initial topography is shown by the black line. (b) – (d) RSLice and RSLwater terms and RSL changes at t = 0, 10, 20, 50 and 70 kyr for the transect (dark gray line) shown in panels (a). (e) – (g) RSLice and RSLwater terms and RSL changes at sites B1 – B7 shown in panel (a). In panel (g), the RSL change predicted at ocean site for the paleotopography is shown by the solid line, and that at land site is shown by the dotted line. The predictions in panels (e) and (f) are shown by solid lines. (h) – (n) As in panels (a) – (g), except for the coastline geometry model M2.

rate after ~20 kyr is spatially uniform. Also, RSL changes at sites B1–B7 after t~20 kyr are nearly identical to those for M0 (Figures 3.12g and 3.12n). These spatial variations in RSL change are explained by considering the interaction between the collapse of the peripheral bulge and local crustal uplift within the peninsula area. We examine these variations by considering the effects of $\mathrm{RSL_{ice}}$ and $\mathrm{RSL_{water}}$ terms on RSL change.

The maximum height of the peripheral bulge at t = 0 kyr moves westward (Figure 3.12k) locally as inferred from the hinge-line movement at sites b1–b7 in Figure 3.12h, and consequently, the peninsula region locally uplifts $t < 20$ kyr. However, the $\mathrm{RSL_{ice}}$ and $\mathrm{RSL_{water}}$ terms for $t > 20$ kyr at sites B1–B7 are insensitive to the coastline geometry model (see Figures 3.12e–3.12f and 3.12l–3.12m), and therefore, the RSL changes after t~20 kyr for M2 are nearly identical to those for M0 (Figures 3.12g and 3.12n). Figure 3.12l shows that the $\mathrm{RSL_{ice}}$ term for $t < 20$ kyr is significantly affected by the melting in the peninsula and the $\mathrm{RSL_{ice}}$ terms at sites B1–B4 monotonically fall for $t > 0$ kyr (see also Figure 3.12e). Also, the $\mathrm{RSL_{water}}$ term for M2 at sites B1–B6 shows a fall in the post-deglacial phase (Figure 3.12m) as is predicted at sites B1–B3 for M0 (Figure 3.12f). These effects for $t < 20$ kyr due to the $\mathrm{RSL_{ice}}$ and $\mathrm{RSL_{water}}$ terms are limited to the peninsula region, and consequently, the

RSL changes at continental shelf sites B2–B6 show a gradual RSL fall in ocean area (Figure 3.12n). That is, the RSL changes at sites B1–B7 for $t \leq 20$ kyr reflect mainly the local crustal uplift and those for $t > 20$ kyr reflect the behavior of the peripheral bulge for $t > 20$ kyr almost identical to that for M0.

We next examine the RSL change for region C based on the coastline geometry model M0 (Figures 3.13a–3.13g). The difference between regions C and B (Figure 3.5a) is due to the spatial scale of the adjacent ocean. Region C faces a relatively small ocean surrounded by continents (ocean "X"). The hinge-line shows an inward migration for $t \geq 0$ kyr and the RSL changes bear similar RSL patterns as shown in Figure 3.9b. The maximum height of the peripheral bulge at $t = 0$ kyr inferred from the RSL change is ~450 m around –6°E (Figure 3.13d) and significantly higher than ~200 m in region B for M0 (Figure 3.12d). Particularly, the height for $\mathrm{RSL_{water}}$ term (Figure 3.13c) is ~250 m (~200 m for $\mathrm{RSL_{ice}}$ term) and significantly higher than ~70 m in region B for M0 (Figure 3.12c). This probably depends on the magnitude of the peripheral bulge at the maximum glaciation and the collapse of the peripheral bulge in the syn- and post-glacial phases. The peripheral bulge at the maximum glaciation is related to the Earth response to the ice loading and seawater unloading, and the collapse of the peripheral bulge in the syn- and post-deglacial phases is caused by the ice-sheet unloading and meltwater loading. That is, the significant contribution of the $\mathrm{RSL_{water}}$ term is probably attributed to the GIA response due to the seawater unloading and meltwater loading with a spatial-scale of ocean "X" (Figure 3.8c). This would be a main cause of the inward migration of the hinge-line for region C responsible for the difference between the RSL changes for regions B and C.

We next examine the RSL change at each site shown in Figures 3.13e–3.13f. The RSL change at inland site C4 shows a monotonic RSL fall, which is largely contributed by the $\mathrm{RSL_{ice}}$ component. Those at ocean sites C7–C11 show a transgression followed by an RSL drop, which is equally contributed by the $\mathrm{RSL_{ice}}$ and $\mathrm{RSL_{water}}$ terms. The RSL changes at ocean sites B4–B7 are, however, mainly due to the $\mathrm{RSL_{ice}}$ term (Figures 3.12b–3.12c and 3.12e–3.12f). The prediction at coastline site C7 shows a gradual transgression until ~100

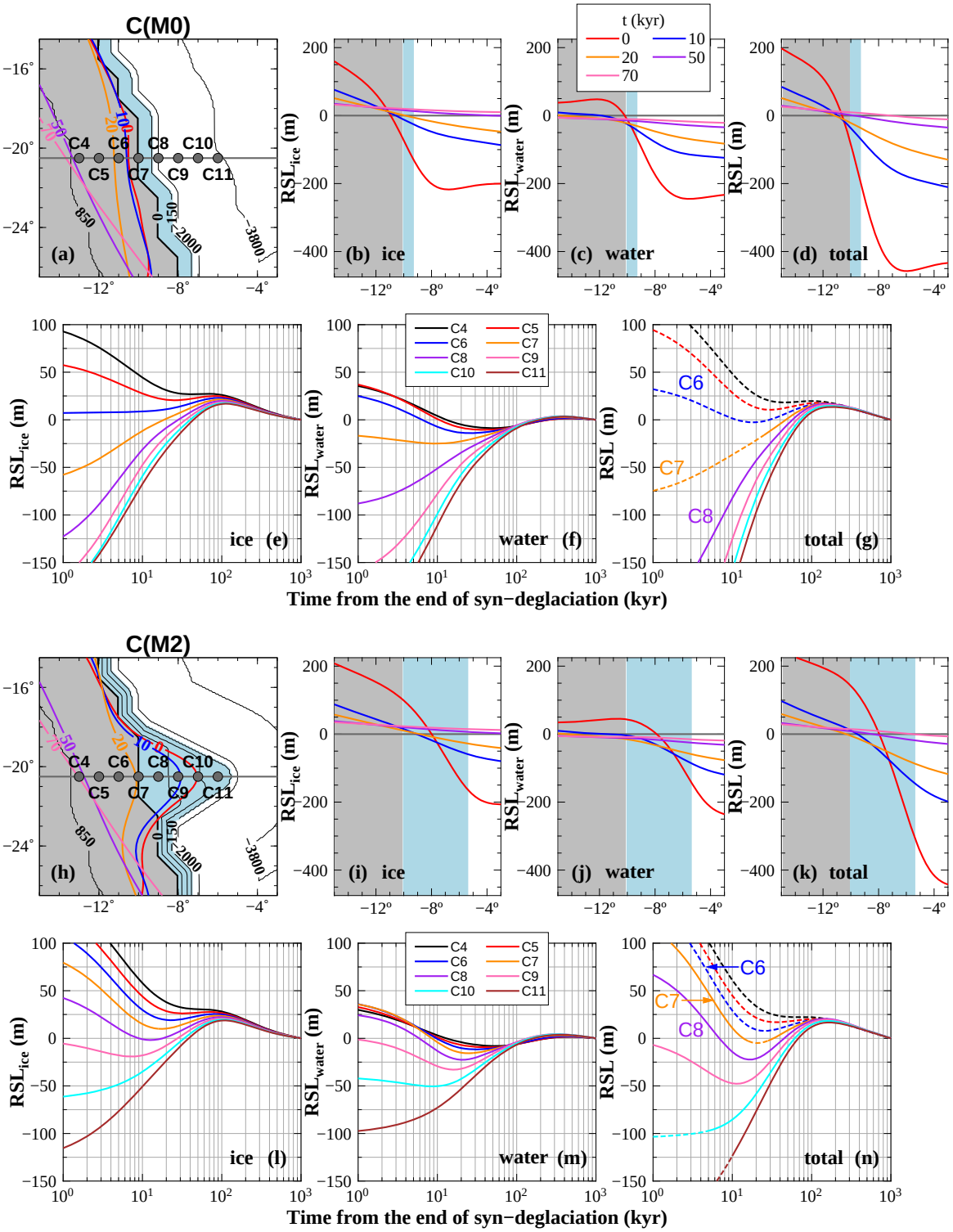

Figure 3.13. As in Figure 3.12, except for region C (see Figure 3.8a).

kyr (on "land area" for $t < 30$ kyr), which is significantly different from that at coastline site B2 (see also RSL changes at sites B3 and C8). Also, the RSL change at site C6 shows a non-monotonic RSL behavior characterized by an RSL drop for $t < 20$ kyr and a transgression for $t > 20$ kyr on "land area", which is mainly contributed by RSL_{water} component (Figure 3.13f). These differences between the RSL changes for regions B and C are related to the crustal movements around their coastline areas that reflect different hinge-line behaviors (Figures 3.12a, 3.13a and 3.8c). Also, we point out that region B, a coastal area in the case of the geometry M0, may be a more suitable depositional place for cap dolostones than that for region C (see RSL changes at sites B2 and C7).

We next consider the RSL changes for region C based on the coastline geometry model M2 (Figures 3.13h–3.13n). The RSL changes for t >20 kyr at all region C sites are nearly identical to those for M0 (Figure 3.13g) as inferred from the hinge-line movements after t~20 kyr for both geometry models (Figures 3.13a and 3.13h). Of course, the RSL_{ice} and RSL_{water} contributions for M2 are nearly the same as those for M0 (Figures 3.13e–3.13f and 3.13l–3.13m). However, the RSL changes at sites C7–C9 located on the continental shelf show a non-monotonic RSL behavior characterized by a significant RSL drop for $t < 20$ kyr followed by a transgression (Figure 3.13n), which reflects the local hinge-line movement in the peninsula region. The RSL_{ice} term for $t < 20$ kyr is significantly affected by the local uplift associated with ice load melting in the peninsula, which contributes to an RSL drop followed by transgression at sites C6–C9 (Figures 3.13l and 3.13n). The RSL_{water} terms at sites C4–C6 (continent sites for the initial topography) are nearly the same as those for M0. However, those at sites C7–C11 for $t < 20$ kyr are significantly larger than those for M0 (Figures 3.13f and 3.13m), which also contributes to an RSL drop followed by transgression at sites C7–C9. Consequently, the RSL changes at sites C7–C9 show an RSL drop followed by transgression for the continental shelf (Figure 3.13n). That is, relaxation processes for $t <$ 20 kyr are controlled primarily by ice load melting with a spatial-scale of the peninsula for M2 (Figures 3.13l–3.13m), and subsequently by the ice-sheet unloading and meltwater loading with a spatial-scale of the ocean "X". The RSL drops occur within ocean area (denoted by the

solid line), and site C7 lies above sea level from 20 to 30 kyr (denoted by the dotted line). We also point out that such non-monotonic post-deglacial RSL behavior would not be expected if we evaluate the RSL change relative to a reference time ~10 kyr after the complete melt, corresponding to the post-deglacial RSL change in the case of the post-LGM deglaciation.

We have also examined the predicted post-deglacial RSL changes for other viscosity models in terms of the monotonic and non-monotonic RSL behaviors described above. The RSL behaviors for M0 and in region B sites for M2 do not change when other viscosity models are considered, although we do not show the results. In region C sites for M2, however, non-monotonic RSL behavior is predicted by several viscosity models. We therefore briefly discuss the post-deglacial RSL changes at region C sites for M2. Figures 3.14b–3.14d show RSL changes at sites C7–C11 for three lower mantle viscosity models. The general feature of the RSL change for $\eta_{lm} = 5 \times 10^{21}$ Pa s (Figure 3.14b) is similar to that for $\eta_{lm} = 10^{22}$ Pa s (Figure 3.14c) and an RSL drop followed by transgression is not evident for these models. Figure 3.14d shows the RSL changes for a two-layer lower mantle viscosity model with $\eta_{670,1191} = 5 \times 10^{21}$ and $\eta_{1191,2891} = 5 \times 10^{22}$ Pa s. This two-layer model predicts an RSL drop followed by transgression at sites C7–C9, a trend that is also predicted for the model with η_{lm} $= 5 \times 10^{22}$ (Figure 3.13n). That is, the sea level peak at ~100 kyr predicted for these two viscosity models, which is largely driven by the ice-sheet unloading and meltwater loading with a spatial-scale of the ocean "X", can be attributed mainly to the viscosity in the deep mantle, i.e., the viscosity below 1191 km depth assumed in this study. Although we only show the results for $T_d = 2$ kyr, the sensitivity of the post-deglacial RSL change to the lower mantle viscosity is also evident for the cases of T_d >2 kyr.

Figures 3.14e–3.14h explore the sensitivities of predicted RSL changes to the lithospheric thickness (H), upper mantle viscosity (η_{um}) and syn-deglacial duration (T_d) in the case of the two-layer lower mantle viscosity model. For the models with $T_d = 2$ and 5 kyr, a post-deglacial RSL drop followed by transgression is predicted for all upper mantle viscosity models. For the models with $T_d = 7.5$ and 10 kyr, however, a non-monotonic RSL behavior is predicted for $4 \times 10^{20} < \eta_{um} \leq 7 \times 10^{20}$ Pa s (Figures 3.14e–3.14g). These results are related

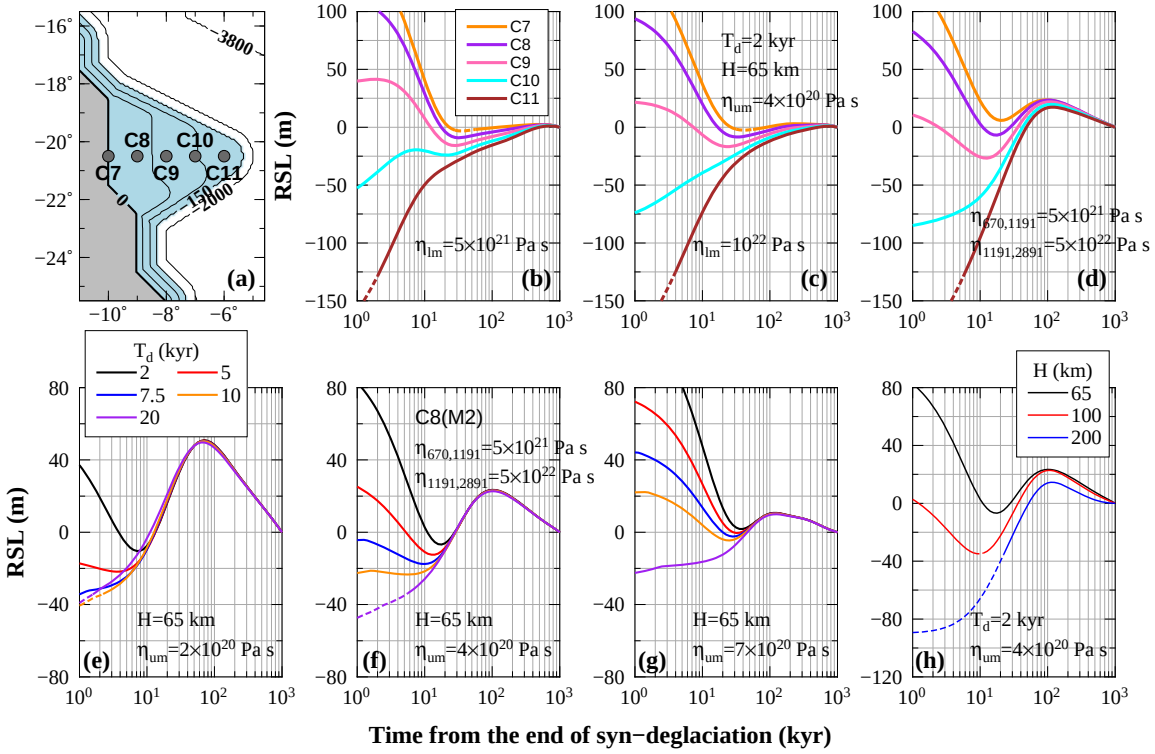

Figure 3.14. (a) An enlarged map for region C with the coastline geometry model M2. The shaded blue region represents the continental shelf for the initial topography and the gray regions represent land areas. The contour line for the initial topography is shown by the black line. (b) – (d) RSL changes at sites C7–C11 in panel (a) for T_d = 2 kyr, H = 65 km and $\eta_{um} = 4 \times 10^{20}$ Pa s (thick line). (b) – (c) RSL changes for simple three-layer viscosity models with η_{lm} = (5, 10) × 10^{21} Pa s and (d) RSL changes for a two-layer lower mantle viscosity model with $\eta_{670,1191} = 5 \times 10^{21}$ and $\eta_{1191,2891} = 5 \times 10^{22}$ Pa s. (e) – (h) RSL changes at site C8 in panel (a) for the two-layer lower mantle viscosity model. (e) – (g) RSL changes for T_d = (2, 5, 7.5, 10, 20) kyr, H = 65 km and η_{um} = (2, 4, 7) × 10^{20} Pa s and (h) RSL changes for T_d = 2 kyr, H = (65, 100, 200) km and $\eta_{um} = 4 \times 10^{20}$ Pa s. The RSL change predicted at ocean site for the paleotopography is shown by the solid line, and that at land site is shown by the dotted line.

to the trade-off between T_d and η_{um} values. In the case of the model with T_d = 10 kyr and $\eta_{um} = 2 \times 10^{20}$ Pa s, for example, the peninsula-scale viscous relaxation occurs largely in the syn-deglacial phase and its related crustal uplift has a negligible impact on the post-deglacial RSL change. Figure 3.14h shows the sensitivity to the lithospheric thickness. The general feature of the RSL change for H = 100 km is similar to that evident for H = 65 km. However, an RSL drop is not predicted for H = 200 km because the crustal deformation with a spatial-scale of peninsula for M2 is elastically supported by the thick lithosphere.

3.4 Discussion

3.4.1 Comparison between sedimentary-inferred and predicted RSL changes

Marinoan cap dolostones are generally accepted to have been deposited during the marine transgression resulting from snowball meltdown (Hoffman & Schrag, 2002). The transgression is mainly caused by an ESL rise in the syn-deglacial phase (e.g. RSL change at site C3 in Figure 3.4b) and by collapse of peripheral bulge in the post-deglacial phase (e.g. RSL change at site B3 in Figure 3.12g), as demonstrated by Creveling and Mitrovica (2014). Indeed, post-meltdown sedimentary records such as cap dolostones appear to reflect transgression alone in, for example, southern Amazon (Nogueira et al., 2007), Zavkhan Terrane of southwestern Mongolia (Bold et al., 2016), Svalbard (Halverson et al., 2004) and East Finnmark of Norway (Rice et al., 2011) (AM, MO, SV and NO in Figure 3.8a, respectively). However, an RSL drop interrupting transgression has been identified in some regions. Stratigraphic records show a syn-deglacial RSL drop in Namibia (Hoffman & Macdonald, 2010) and South Australia (Rose et al., 2013) (NA and SA in Figure 3.8a, respectively). Creveling and Mitrovica (2014) indicated that such a syn-deglacial RSL drop may be attributed to one of the three processes (or their combination) of rapid localized (asynchronous) melting during a global stasis in melting, crustal uplift in regions previously under significant ice cover, and an extended syn-deglacial phase of duration ~50 kyr or greater. In this study, syn-deglacial RSL drop is

predicted at the continental slope site for the coastline geometry models M1 and M2 (Figure 3.4). This is related to the second process discussed by Creveling and Mitrovica (2014).

On the other hand, non-monotonic RSL behavior in the post-deglacial phase characterized by an RSL drop and a resumed transgression has been inferred from cap dolostones on the continental shelf of locations such as the South China. Our numerical experiments indicate that the non-monotonic post-deglacial RSL behavior is sensitive to the syn-deglacial duration, mantle viscosity structure and paleogeography. That is, it may be possible to put some constraints on these model parameters by comparing sedimentary-inferred and predicted RSL changes at different sites. Any such inferences are bound to be preliminary given the sparsity of observationally inferred RSL changes and uncertainties in GIA modeling parameters associated with melting histories and paleogeography. However, the following discussion is valid even if we adopt a rapid localized melting event. That is, a rapid localized melting event has a minor impact on the post-deglacial RSL change because this change is mainly driven by the relaxation process due to the continent-scale deglaciation rather than by the localized melting. It is also noted that the post-deglacial RSL change in South China, which is significantly affected by Earth's rotational response to Marinoan snowball meltdown, is thus mainly sensitive to gross melting history.

Zhou et al. (2010) inferred an RSL change with a syn-deglacial transgression followed by an RSL drop and a transgression in the post-deglacial phase based on the stratigraphic studies of cap dolostones in South China (SC in Figure 3.8a). They interpreted the karst-like dissolution features at the top of the cap dolostones as a brief interval of RSL drop, which are common throughout most of the platform, shelf, and even shallow basinal facies in South China. Over the continental shelf area between sites A1 and A2 (Figure 3.10a), syn-deglacial transgression followed by an RSL drop and transgression in the post-deglacial phase is predicted for models with a viscosity of 5×10^{22} Pa s in the deep mantle and $T_d \leq 20$ kyr regardless of the adopted upper mantle viscosity and lithospheric thickness (Figure 3.10). The predicted RSL change is consistent with the inferred RSL change in South China although only the coastal region between sites A1 and A4 (Figure 3.10a) undergoes subaerial

exposure.

The cap dolostones on shelf sections in Mackenzie Mountains, northwestern Canada (James et al., 2001) (MM in Figure 3.8a) and on the topographic highs in West Africa (Bertrand-Sarfati et al., 1997; Shields et al., 2007) (WA in Figure 3.8a) suggest similar sedimentary features as those of the cap carbonate sequences in South China. Also, the cap carbonate platform in California (CA in Figure 3.8a) records karstic features (Creveling et al., 2016). The karst features at these sites have been interpreted as an RSL drop in the syn-deglacial phase due to glacial rebound. However, our numerical experiments do not predict the syn-deglacial RSL drop for ocean sites of the continental shelf because the continental shelf lies above sea level until the late stage of the syn-deglacial phase. However, our model suggests that the inferred RSL drop may have occurred during the post-deglacial phase, which is consistent with the cap dolostones at these sites bearing no ice-rafted debris. Differing from South China, the RSL changes of Canada and California sites had a negligible signal from Earth's rotation because they were at equatorial regions. The same may be true for the West Africa site (see Figure 3.5d).

Our numerical experiments indicate that non-monotonic post-deglacial RSL behavior requires the following two paleogeographic conditions: (i) an adjacent ocean such as the ocean "X" or oceans (gulfs) indicated by arrows in Figure 3.8c; and (ii) a wide continental shelf such as M2 (Figure 3.13h). We therefore discuss the RSL drop at these sites based on the post-deglacial RSL changes at continental shelf site C8 for the geometry model M2 (Figure 3.13h). We found that an RSL drop followed by transgression in the post-deglacial phase is evident for models with a viscosity of 5×10^{22} Pa s in the deep mantle and $T_d < 20$ kyr, but also depends on the upper mantle viscosity (Figure 3.14). It should be noted that the predicted RSL change in region C is significantly affected by the subsidence of the ocean "X" due to the ice-sheet unloading and meltwater loading. The northwestern Canada (MM) and West Africa (WA) sites (Figure 3.8a), which face an ocean (gulf) indicated by arrows in Figure 3.8c, show non-monotonic RSL behaviors for the coastline geometry model M2 as inferred from the RSL changes for region C (Figures 3.8, 3.13 and 3.14). Also, it may be possible to

assume that the paleogeography around the California (CA) site (Figure 3.8a) had a comparable geometry to that for region C if we consider uncertainties of the paleogeography (see paleogeography around California site).

The non-monotonic post-deglacial RSL behavior inferred from the sedimentary records worldwide may be explained by a synchronous melting model with $T_d < 20$ kyr and a deep mantle viscosity of $\sim 5 \times 10^{22}$ Pa s. A discussion of Neoproterozoic mantle viscosity is challenging if we consider the thermal history of the Earth (e.g. Ganne & Feng, 2017) and its impact on the mantle viscosity (Karato, 2008). Nevertheless, a deep mantle viscosity of $\sim 5 \times 10^{22}$ Pa s may be consistent with an estimate of $\sim 10^{23}$ Pa s inferred from the recent analyses using GIA data sets pertinent to the last deglaciation (Lau et al., 2016; Nakada & Okuno, 2016; Nakada et al., 2018). According to the results of Ganne and Feng (2017), for example, the average temperature of the mantle at 0.6–0.7 Gyr was ~50 K higher than at present. This may suggest that the Neoproterozoic mantle viscosity is approximately half of the present one for an assumed temperature distribution by Nakada et al. (2018). Nakada et al. (2018) examined the GIA-related observations such as RSL changes and secular rate of change of the degree-two zonal harmonic of the geopotential, $\dot{J}_2$, based on the temperature-dependent viscosity model. Although the results are not shown here, the non-monotonic post-deglacial RSL behavior inferred from the sedimentary records worldwide can be explained based on the viscosity model with temperature distribution ~50 K higher than the deep mantle viscosity of 10^{23} Pa s and average upper mantle viscosity of 4×10^{20} Pa s preferred by Nakada et al. (2018) (see Figure 1.3). A post-deglacial RSL drop followed by transgression is also predicted for the viscosity model with an upper mantle viscosity of 10^{20} Pa s and lithospheric thickness of 50 km as inferred from the results shown in Figures 3.10e–h and 3.14e–h.

Finally, we discuss the syn-deglacial duration. The numerous positive feedbacks in the climate system suggest that once deglaciation begins, it proceeds rapidly to a globally ice-free state (Pierrehumbert et al., 2011; Hoffman et al., 2017). The duration of ~2 kyr has been inferred from ice sheet dynamics (Hyde et al., 2000). For a melting model with $T_d \sim 2$ kyr, syn-deglacial RSL drop would be predicted in the case of a melting model with a rapid

localized melting event (Creveling & Mitrovica, 2014). More recently, Myrow et al. (2018) examined a rate of sea level rise during the deglaciation based on a paleohydraulic analysis of wave ripples and tidal laminae for ~100 yr sediment records of the Elatina Formation, South Australia (SA in Figure 2a), and estimated a rate equivalent to a syn-deglacial duration of ~6 kyr. Our estimate of $T_d < 20$ kyr inferred from non-monotonic RSL behavior in the post-deglacial phase is not inconsistent with these estimates, but we cannot put a tight constraint on the syn-deglacial duration.

3.4.2 Inference of MOSD duration

Our modeling exercise allows us to place some constraints on the duration of the MOSD event, a transient episode of extremely ^{17}O-depleted atmospheric O_2, recorded in the sediments immediate after the onset of the Marinoan meltdown. Figure 3.15a shows Marinoan cap dolostone sections on South China craton (Zhou et al., 2010; Jiang et al., 2011; Killingsworth et al., 2013), and Figure 3.15b shows the Nantuo diamictites and a basal Ediacaran stratigraphic sequence at Wushanhu (section 12 in Figure 3.15a), Hubei Province, China. Zhou et al. (2010) and Killingsworth et al. (2013) define the cap carbonates as the carbonates overlying the Nantuo diamictite that deposited before the occurrence of a disrupted (dissolution or karst) surface that hosts barite crystal fans. The disrupted features at the top of the cap carbonates are common throughout most of the platform, shelf, and even shallow basinal facies in South China (Zhou et al., 2010) (section 1–11 in Figure 3.15a). Therefore, if we can correlate the sedimentologically-inferred sea level change to the Wushanhu section where the MOSD has been pinned to the post-meltdown sedimentary sequence (Killingsworth et al., 2013) (section 12 in Figure 3.15a), we can provide an independent estimate of the duration of the cap carbonate deposition, the timing of the barite fan deposition, and the duration of the MOSD event, based on our modeled RSL pattern and durations. The MOSD signature is recorded by sulfate deposits such as the unusual barite fans (Bao et al., 2008). Since the MOSD window is not coeval with the time of the highest pCO_2 when the meltdown began but rather a time when the atmospheric O_2 and CO_2 had comparable concentrations (Cao &

Bao, 2013), the MOSD duration can provide an important constraint on the rates of pCO_2 drawdown by weathering and pO_2 rise due to biological recovery and organic burial in the aftermath of Marinoan snowball meltdown.

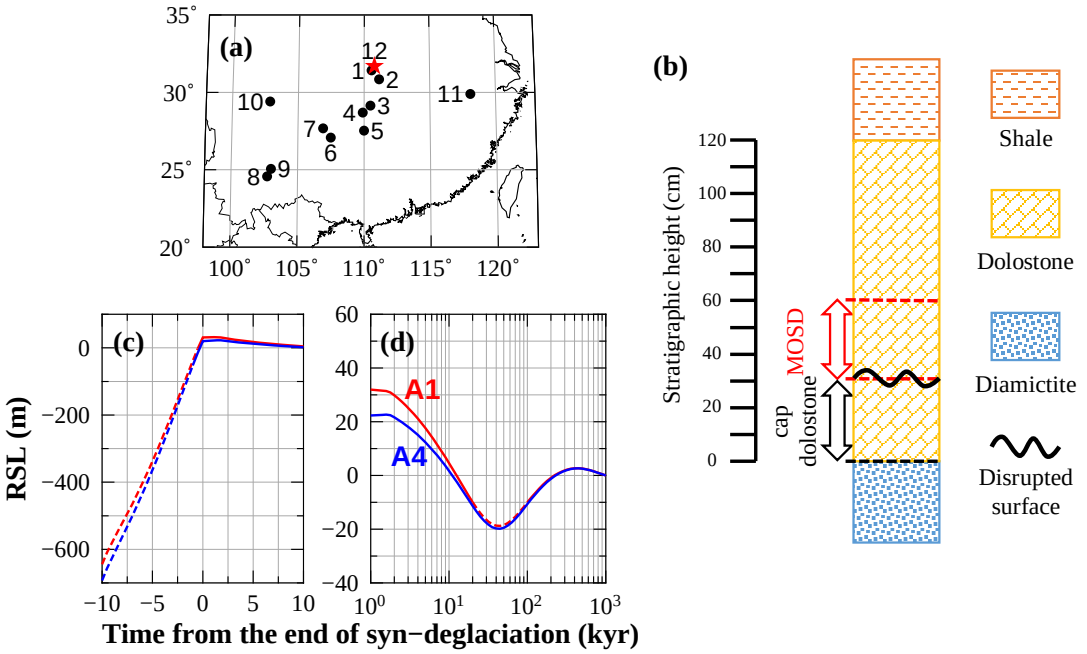

Figure 3.15. (a) Marinoan cap dolostone sections on South China (or Yangtze) craton: sections 1–11 investigated by Zhou et al. (2010) and section 12 investigated by Killingsworth et al. (2013). (b) The post-Marinoan or basal Ediacaran stratigraphic sequence at Wushanhu (section 12), Hubei Province, China (modified from Killingsworth et al. 2013). (c) – (d) Syn- and post-deglacial RSL changes at sites A1 and A4 (Figure 3.10a) for the model with T_d = 10 kyr, H = 65 km, $\eta_{um} = 4 \times 10^{20}$, $\eta_{670,1191} = 5 \times 10^{21}$ and $\eta_{1191,2891} = 5 \times 10^{22}$ Pa s. The RSL change predicted at ocean site for the paleotopography is shown by the solid line, and that at land site is shown by the dotted line.

Figures 3.15c–3.15d show the RSL changes at sites A1 and A4 (Figure 3.10a) based on the model with T_d = 10 kyr (see also Figure 3.10). The Nantuo diamictites should have been deposited by the end of the syn-deglacial transgression. If the predicted post-deglacial RSL

drop or regression-transgression transition occurred at the top of the cap carbonates or at the onset of the barite fan deposition, the inferred period for cap carbonate deposition (Figure 3.15b) would be ~50 kyr (Figure 3.15d). Also, if we assume that the deposition of the cap carbonates in South China started at the end of syn-deglacial phase, the maximum duration of the cap carbonate deposition would also be ~50 kyr. If an equal deposition rate for the cap dolostones and the overlying dolostones, where the MOSD period resides, is assumed, the maximum duration of the MOSD is also estimated to be also ~50 kyr. If we consider Le Hir et al.'s (2008) ocean chemistry constraint that it would take a minimum of 20 kyr to bring the ocean alkalinity to the level of carbonate precipitation via continental weathering, then the corresponding durations of the cap carbonate deposition and the MOSD event will both be 30 kyr. These estimates are consistent with the previous estimate of a < 1 Myr duration for the MOSD event, as inferred independently from two radiometric dates for nearby sections correlated to the Wushanhu section (Killingsworth et al., 2013), and also from a coupled, four-box and quick-response biosphere-atmosphere model (Cao and Bao, 2013). Added the <20 kyr syn-deglacial duration, the total duration starting from the onset of deglaciation to the end of the MOSD episode is within 100 kyr. The 100 kyr is therefore the total time the post-Marinoan Earth took to draw a pCO_2 at >100 present atmospheric level down to a level within 1-2 magnitudes of present atmospheric level.

3.5 Conclusions

Marinoan snowball Earth offers us a set of sedimentary and geochemical records for exploring GIA associated with one of the most severe glaciations in Earth history. Moreover, an accurate prediction of GIA-based RSL change associated with a snowball Earth will help to interrogate sedimentary records to place constraints on mantle viscosity structure, the paleogeographic details associated with cap carbonate deposition, and the durations of syn-deglaciation and cap carbonate deposition. We have assumed a globally synchronous melting for all ice sheets and have evaluated GIA-based RSL changes by considering the impacts of paleotopography and coastline geometry on inferred GIA model parameters. The main pur-

pose of this study is to discuss the post-deglacial RSL change characterized by an RSL drop followed by a transgression inferred from sedimentary records such as those in South China (Zhou et al., 2010). This is because such a non-monotonic RSL behavior may be a diagnostic suggesting that the Marinoan deglaciation was characterized by a significantly longer post-deglacial GIA-response than the last deglaciation. A post-deglacial RSL drop followed by transgression in South China, which is significantly impacted by changes in Earth's rotation, is predicted over the continental shelf area for models with $T_d \leq 20$ kyr and a deep mantle viscosity of $\sim 5 \times 10^{22}$ Pa s regardless of the adopted upper mantle viscosity and lithospheric thickness (Figure 3.10). On the other hand, post-deglacial RSL changes at low-latitude regions (e.g. NA, MM and CA sites in Figure 3.8a), having a negligible RSL contribution from Earth rotation, are driven largely by the collapse of the peripheral bulge and also by paleogeographic considerations, such as the scale of adjacent ocean and size of the continental shelf. Our GIA modeling of the RSL change in South China also explains the sedimentary-inferred RSL drops on the continental shelf in northwestern Canada (James et al., 2001) and California (Creveling et al., 2016) if these sites were adjacent to an ocean such as the ocean "X" (oceans in Figure 3.8c indicated by arrows) and located on a wide continental shelf such as in the geometry model M2 (Figures 3.13 and 3.14). Furthermore, the good match between the predicted and the observed RSL change in South China suggests an approximate duration of ~50 kyr for the Marinoan ^{17}O depletion event, an atmospheric event linked to the post-Marinoan drawdown of CO_2 and the concurrent rise of O_2 (Figure 3.15).

Acknowledgements

I appreciate my supervisor Prof. Masao Nakada for much support and encouragement in my study. Also I appreciate Shigeo Yoshida, Jun'ichi Okuno and Huiming Bao for support through this study. I thank Satoshi Kaneshima and Hiroshi Shimizu for their constructive comments and Ryosuke Nakashima for valuable discussion and encouragement. I also thank Hiroyoshi Sano for helpful discussion and members of geodynamics group for useful advice.

References

Bao, H., Lyons, J. R., & Zhou, C. (2008). Triple oxygen isotope evidence for elevated CO_2 levels after a Neoproterozoic glaciation. *Nature*, *453*(7194), 504–506. https://doi.org/10.1038/nature06959

Bertrand-Sarfati, J., Flicoteaux, R., Moussine-Pouchkine, A., & Ait Kaci Ahmed, A. (1997). Lower Cambrian apatitic stromatolites and phospharenites related to the glacio-eustatic cratonic rebound (Sahara, Algeria). *Journal of Sedimentary Research*, *67*(5), 957–974. https://doi.org/10.1306/D426868A-2B26-11D7-8648000102C1865D

Bold, U., Smith, E. F., Rooney, A. D., Bowring, S. A., Buchwaldt, R., Dudás, F. O., et al. (2016). Neoproterozoic stratigraphy of the Zavkhan terrane of Mongolia: The backbone for Cryogenian and early Ediacaran chemostratigraphic records. *American Journal of Science*, *316*(11), 1–63. https://doi.org/10.2475/01.2016.01

Cao, X., & Bao, H. (2013). Dynamic model constraints on oxygen-17 depletion in atmospheric O_2 after a snowball Earth. *Proceedings of the National Academy of Sciences*, *110*(36), 14546–14550. https://doi.org/10.1073/pnas.1302972110

Cathles, L. M. (1975). *The viscosity of the Earth's Mantle*. Princeton: Princeton University Press.

Chinnery, M. A. (1975). The Static Deformation of an Earth with a Fluid Core: A Physical Approach. *Geophysical Journal of the Royal Astronomical Society*. https://doi.org/10.1111/j.1365-246X.1975.tb05872.x

Clark, J. A. (1976). Greenland's rapid postglacial emergence: A result of ice-water gravitational attraction. *Geology*, *4*(5), 310–312. https://doi.org/10.1130/0091-7613(1976)4<310:GRPEAR>2.0.CO;2

Creveling, J. R., Bergmann, K. D., & Grotzinger, J. P. (2016). Cap carbonate platform facies model, Noonday Formation, SE California. *Bulletin of the Geological Society of America*, *128*(7), 1249–1269. https://doi.org/10.1130/B31442.1

Creveling, J. R., & Mitrovica, J. X. (2014). The sea-level fingerprint of a Snowball Earth deglaciation. *Earth and Planetary Science Letters*, *399*, 74–85. https://doi.org/10.1016/j.epsl.2014.04.029

Dziewonski, A. M., & Anderson, D. L. (1981). Preliminary reference Earth model. *Physics of the Earth and Planetary Interiors*, *25*(4), 297–356. https://doi.org/10.1016/0031-9201(81)90046-7

Farrell, W. E., & Clark, J. A. (1976). On postglacial sea level. *Geophysical Journal of the Royal Astronomical Society*, *46*(3), 647–667. https://doi.org/10.1111/j.1365-246X.1976.tb01252.x

Forte, A. M., Simmons, N. A., & Grand, S. P. (2015). Constraints on Seismic Models from Other Disciplines - Constraints on 3-D Seismic Models from Global Geodynamic Observables: Implications for the Global Mantle Convective Flow. In *Treatise on Geophysics: Second Edition*. https://doi.org/10.1016/B978-0-444-53802-4.00028-2

Ganne, J., & Feng, X. (2017). Primary magmas and mantle temperatures through time. *Geochemistry, Geophysics, Geosystems*, *18*(3), 872–888. https://doi.org/10.1002/2016GC006787

Goldstein, H. (1980). *Classical Mechanics*. Boston: Addison-Wesley.

Halverson, G. P., Maloof, A. C., & Hoffman, P. F. (2004). The Marinoan glaciation (Neoproterozoic) in northeast Svalbard. *Basin Research*, *16*(3), 297–324. https://doi.org/10.1111/j.1365-2117.2004.00234.x

Hoffman, P. F. (2011). Strange bedfellows: glacial diamictite and cap carbonate from the Marinoan (635 Ma) glaciation in Namibia. *Sedimentology*, *58*(1), 57–119. https://doi.org/10.1111/j.1365-3091.2010.01206.x

Hoffman, P. F., Abbot, D. S., Ashkenazy, Y., Benn, D. I., Brocks, J. J., Cohen, P. A., et al. (2017). Snowball Earth climate dynamics and Cryogenian geology-geobiology. *Science Advances*, *3*(11), e1600983. https://doi.org/10.1126/sciadv.1600983

Hoffman, P. F., Halverson, G. P., Domack, E. W., Husson, J. M., Higgins, J. A., & Schrag, D. P. (2007). Are basal Ediacaran (635 Ma) post-glacial “cap dolostones” diachronous? *Earth and Planetary Science Letters*, *258*(1–2), 114–131. https://doi.org/10.1016/j.epsl.2007.03.032

Hoffman, P. F., & Li, Z. X. (2009). A palaeogeographic context for Neoproterozoic glaciation. *Palaeogeography, Palaeoclimatology, Palaeoecology*, *277*(3–4), 158–172. https://doi.org/10.1016/j.palaeo.2009.03.013

Hoffman, P. F., & Macdonald, F. A. (2010). Sheet-crack cements and early regression in Marinoan (635Ma) cap dolostones: Regional benchmarks of vanishing ice-sheets? *Earth and Planetary Science Letters*, *300*(3–4), 374–384. https://doi.org/10.1016/j.epsl.2010.10.027

Hoffman, P. F., & Schrag, D. P. (2002). The snowball Earth hypothesis: testing the limits of global change. *Terra Nova*, *14*(3), 129–155. https://doi.org/10.1046/j.1365-3121.2002.00408.x

Hyde, W. T., Crowley, T. J., Baum, S. K., & Peltier, W. R. (2000). Neoproterozoic “snowball earth” simulations with a coupled climate/ice- sheet model. *Nature*, *405*(6785), 425–429. https://doi.org/10.1038/35013005

Irie, Y., Nakada, M., Okuno, J., & Bao, H. (2019). Nonmonotonic Postdeglacial Relative Sea Level Changes at the Aftermath of Marinoan (635 Ma) Snowball Earth Meltdown. *Journal of Geophysical Research: Solid Earth*. https://doi.org/10.1029/2018jb017260

James, N. P., Narbonne, G. M., & Kyser, T. K. (2001). Late Neoproterozoic cap carbonates: Mackenzie Mountains, northwestern Canada: precipitation and global glacial meltdown. *Canadian Journal of Earth Sciences*, *38*(8), 1229–1262. https://doi.org/10.1139/cjes-38-8-1229

Jiang, G., Shi, X., Zhang, S., Wang, Y., & Xiao, S. (2011). Stratigraphy and paleogeography of the Ediacaran Doushantuo Formation (ca. 635-551Ma) in South China. *Gondwana Research*. https://doi.org/10.1016/j.gr.2011.01.006

Johnston, P., Lambeck, K., & Wolf, D. (1997). Material versus isobaric internal boundaries in the Earth and their influence on postglacial rebound. *Geophysical*

Journal International, *129*(2), 252–268. https://doi.org/10.1111/j.1365-246X.1997.tb01579.x

Karato, S. (2008). *Deformation of earth materials: An introduction to the rheology of solid earth*. Cambridge: Cambridge University Press.

Killingsworth, B. A., Hayles, J. A., Zhou, C., & Bao, H. (2013). Sedimentary constraints on the duration of the Marinoan Oxygen-17 Depletion (MOSD) event. *Proceedings of the National Academy of Sciences*, *110*(44), 17686–17690. https://doi.org/10.1073/pnas.1213154110

Kilner, B., Mac Niocaill, C., & Brasier, M. (2005). Low-latitude glaciation in the Neoproterozoic of Oman. *Geology*, *33*(5), 413–416. https://doi.org/10.1130/G21227.1

Lambeck, K. (1993). Glacial rebound of the British Isles—I. Preliminary model results. *Geophysical Journal International*, *115*(3), 941–959. https://doi.org/10.1111/j.1365-246X.1993.tb01503.x

Lambeck, K. (1997). Sea-level change along the French Atlantic and Channel coasts since the time of the Last Glacial Maximum. *Palaeogeography, Palaeoclimatology, Palaeoecology*, *129*(1–2), 1–22. https://doi.org/10.1016/S0031-0182(96)00061-2

Lambeck, K., Rouby, H., Purcell, A., Sun, Y., & Sambridge, M. (2014). Sea level and global ice volumes from the Last Glacial Maximum to the Holocene. *Proceedings of the National Academy of Sciences*, *111*(43), 15296–15303. https://doi.org/10.1073/pnas.1411762111

Lambeck, K., & Johnston, P. (1998). The viscosity of the mantle: evidence from analyses of glacial-rebound phenomena. In I. Jackson (Ed.), *The Earth's Mantle: Composition, Structure, and Evolution* (pp. 461–502). Cambridge: Cambridge University Press.

Lambeck, K., Purcell, A., Johnston, P., Nakada, M., & Yokoyama, Y. (2003). Water-load definition in the glacio-hydro-isostatic sea-level equation. *Quaternary Science Reviews*, *22*(2–4), 309–318. https://doi.org/10.1016/S0277-3791(02)00142-7

Lambeck, K., Purcell, A., & Zhao, S. (2017). The North American Late Wisconsin ice sheet and mantle viscosity from glacial rebound analyses. *Quaternary Science Reviews*, *158*, 172–210. https://doi.org/10.1016/j.quascirev.2016.11.033

Le Hir, G., Goddéris, Y., Donnadieu, Y., & Ramstein, G. (2008). A geochemical modelling study of the evolution of the chemical composition of seawater linked to a "'snowball'" glaciation. *Biogeosciences*, *5*(1), 253–267. https://doi.org/10.5194/bg-5-253-2008

Li, Z. X., Evans, D. A. D., & Halverson, G. P. (2013). Neoproterozoic glaciations in a revised global palaeogeography from the breakup of Rodinia to the assembly of Gondwanaland. *Sedimentary Geology*, *294*, 219–232. https://doi.org/10.1016/j.sedgeo.2013.05.016

Liu, Y., & Peltier, W. R. (2013). Sea level variations during snowball Earth formation: 1. A preliminary analysis. *Journal of Geophysical Research: Solid Earth*, *118*(8), 4410–4424. https://doi.org/10.1002/jgrb.50293

Longman, I. M. (1962). A Green's function for determining the deformation of the Earth under surface mass loads: 1. Theory. *Journal of Geophysical Research*. https://doi.org/10.1029/jz067i002p00845

Milne, G. A., Mitrovica, J. X., & Davis, J. L. (1999). Near-field hydro-isostasy: The implementation of a revised sea-level equation. *Geophysical Journal International*, *139*(2), 464–482. https://doi.org/10.1046/j.1365-246X.1999.00971.x

Milne, G. A., & Mitrovica, J. X. (1996). Postglacial sea-level change on a rotating Earth: first results from a gravitationally self-consistent sea-level equation. *Geophysical Journal International*, *126*(3), F13–F20. https://doi.org/https://doi.org/10.1111/j.1365-246X.1996.tb04691.x

Milne, G. A., & Mitrovica, J. X. (1998). Postglacial sea-level change on a rotating Earth. *Geophysical Journal International*, *133*(1), 1–19. https://doi.org/10.1046/j.1365-246X.1998.1331455.x

Mitrovica, J. X., & Forte, A. M. (2004). A new inference of mantle viscosity based upon joint inversion of convection and glacial isostatic adjustment data. *Earth and Planetary Science Letters*, *225*(1–2), 177–189. https://doi.org/10.1016/j.epsl.2004.06.005

Mitrovica, J. X., & Milne, G. A. (2002). On the origin of late Holocene sea-level highstands within equatorial ocean basins. *Quaternary Science Reviews*. https://doi.org/10.1016/S0277-3791(02)00080-X

Mitrovica, J. X., & Wahr, J. (2011). Ice Age Earth Rotation. *Annual Review of Earth and Planetary Sciences*, *39*(1), 577–616. https://doi.org/10.1146/annurev-earth-040610-133404

Mitrovica, J. X., Wahr, J., Matsuyama, I., & Paulson, A. (2005). The rotational stability of an ice-age earth. *Geophysical Journal International*, *161*(2), 491–506. https://doi.org/10.1111/j.1365-246X.2005.02609.x

Munk, W. H., & MacDonald, G. J. F. (1960). *The rotation of the earth*. Cambridge: Cambridge University Press.

Myrow, P. M., Lamb, M. P., & Ewing, R. C. (2018). Rapid sea level rise in the aftermath of a neoproterozoic snowball earth. *Science*, *360*(6389), 649–651. https://doi.org/10.1126/science.aap8612

Nakada, M. (2009). Polar wander of the earth associated with the quaternary glacial cycle on a convecting mantle. *Geophysical Journal International*. https://doi.org/10.1111/j.1365-246X.2009.04289.x

Nakada, M., & Lambeck, K. (1987). Glacial rebound and relative sea-level variations: a new appraisal. *Geophysical Journal of the Royal Astronomical Society*, *90*(1), 171–224. https://doi.org/10.1111/j.1365-246X.1987.tb00680.x

Nakada, M., & Lambeck, K. (1991). Late Pleistocene and Holocene Sea-Level Change; Evidence for Lateral Mantle Viscosity Structure? In R. Sabadini, K. Lambeck, & E. Boschi (Eds.), *Glacial Isostasy, Sea-Level and Mantle Rheology* (pp. 79–94). Dordrecht: Springer. https://doi.org/10.1007/978-94-011-3374-6_5

Nakada, M., & Lambeck, K. (1989). Late Pleistocene and Holocene sea-level change in the Australian region and mantle rheology. *Geophysical Journal International*, *96*(3), 497–517. https://doi.org/10.1111/j.1365-246X.1989.tb06010.x

Nakada, M., & Okuno, J. (2016). Inference of mantle viscosity for depth resolutions of GIA observations. *Geophysical Journal International*, *207*(2), 719–740. https://doi.org/10.1093/gji/ggw301

Nakada, M., Okuno, J., & Irie, Y. (2018). Inference of viscosity jump at 670 km depth and lower mantle viscosity structure from GIA observations. *Geophysical Journal International*, *212*(3), 2206–2225. https://doi.org/10.1093/gji/ggx519

Nakada, M., Okuno, J., & Yokoyama, Y. (2016). Total meltwater volume since the Last Glacial Maximum and viscosity structure of Earth's mantle inferred from relative sea level changes at Barbados and Bonaparte Gulf and GIA-induced J2. *Geophysical Journal International*, *204*(2), 1237–1253. https://doi.org/10.1093/gji/ggv520

Nogueira, A. C. R., Riccomini, C., Sial, A. N., Moura, C. A. V., Trindade, R. I. F., & Fairchild, T. R. (2007). Carbon and strontium isotope fluctuations and paleoceanographic changes in the late Neoproterozoic Araras carbonate platform, southern Amazon craton, Brazil. *Chemical Geology*, *237*(1–2), 168–190. https://doi.org/10.1016/j.chemgeo.2006.06.016

Paterson, W. S. B. (1969). *The physics of glaciers*. Oxford: Pergamon Press.

Pierrehumbert, R. T., Abbot, D. S., Voigt, A., & Koll, D. (2011). Climate of the Neoproterozoic. *Annual Review of Earth and Planetary Sciences*, *39*(1), 417–460. https://doi.org/10.1146/annurev-earth-040809-152447

Rice, A. H. N., Edwards, M. B., Hansen, T. A., Arnaud, E., & Halverson, G. P. (2011). Glaciogenic rocks of the Neoproterozoic Smalfjord and Mortensnes formations, Vestertana Group, E. Finnmark, Norway. In E. Arnaud, G. P. Halverson, & G. A. Shields-Zhou (Eds.), *Geological Society, London, Memoirs* (Vol. 36, pp. 593–602). London: Geological Society of London. https://doi.org/10.1144/M36.57

Rose, C. V., Maloof, A. C., Schoene, B., Ewing, R. C., Linnemann, U., Hofmann, M., & Cottle, J. M. (2013). The end-Cryogenian glaciation of South Australia. *Geoscience Canada*, *40*(4), 256–293. https://doi.org/10.12789/geocanj.2013.40.019

Sabadini, R., Vermeersen, B., & Cambiotti, G. (2016). *Global Dynamics of the Earth: Applications of Viscoelastic Relaxation Theory to Solid-Earth and Planetary Geophysics*. Dordrecht: Springer. https://doi.org/10.1007/978-94-017-7552-6

Shields, G. A., Deynoux, M., Strauss, H., Paquet, H., & Nahon, D. (2007). Barite-bearing cap dolostones of the Taoudéni Basin, northwest Africa: Sedimentary and

isotopic evidence for methane seepage after a Neoproterozoic glaciation. *Precambrian Research*, *153*(3–4), 209–235. https://doi.org/10.1016/j.precamres.2006.11.011

Trindade, R. I. F., Font, E., D'Agrella-Filho, M. S., Nogueira, A. C. R., & Riccomini, C. (2003). Low-latitude and multiple geomagnetic reversals in the Neoproterozoic Puga cap carbonate, Amazon craton. *Terra Nova*, *15*(6), 441–446. https://doi.org/10.1046/j.1365-3121.2003.00510.x

Tushingham, A. M., & Peltier, W. R. (1991). Ice-3G: a new global model of Late Pleistocene deglaciation based upon geophysical predictions of post-glacial relative sea level change. *Journal of Geophysical Research*, *96*(B3), 4497–4523. https://doi.org/10.1029/90jb01583

Wolf, D. (1985). On Boussinesq's problem for Maxwell continua subject to an external gravity field. *Geophysical Journal of the Royal Astronomical Society*. https://doi.org/10.1111/j.1365-246X.1985.tb05091.x

Wu, P., & Peltier, W. R. (1982). Viscous gravitational relaxation. *Geophysical Journal of the Royal Astronomical Society*. https://doi.org/10.1111/j.1365-246X.1982.tb04976.x

Zhou, C., Bao, H., Peng, Y., & Yuan, X. (2010). Timing the deposition of 17O-depleted barite at the aftermath of Nantuo glacial meltdown in South China. *Geology*, *38*(10), 903–906. https://doi.org/10.1130/G31224.1